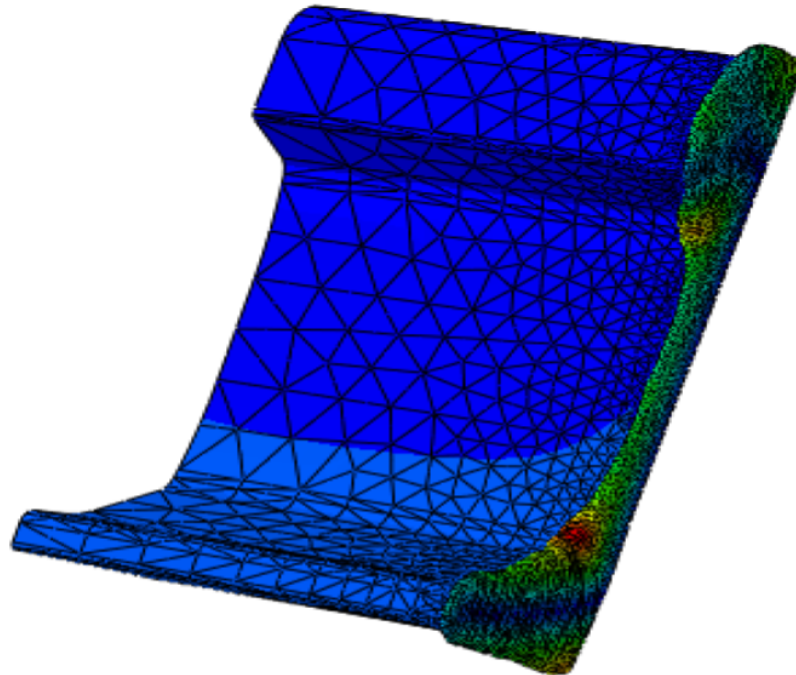




**CHALMERS**  
UNIVERSITY OF TECHNOLOGY

---



# FE modeling of friction welding

Thermo-mechanical simulations using ABAQUS

Master's thesis in Applied mechanics

Clas Thorsell Håkan Ringius



MASTER'S THESIS 2017:06

# FE modeling of friction welding

Thermo-mechanical simulations using ABAQUS

Håkan Ringius  
Clas Thorsell



Department of Applied mechanics  
*Division of material and computational mechanics*  
WRIST  
CHALMERS UNIVERSITY OF TECHNOLOGY  
Gothenburg, Sweden 2017

FE modeling of friction welding  
Thermo-mechanical simulations using ABAQUS  
Håkan Ringius  
Clas Thorsell

© Håkan Ringius, Clas Thorsell, 2017.

Supervisor: Lennart, Department of applied mechanics  
Examiner: Jim, Department of applied mechanics

Master's Thesis 2017:06  
Department of applied mechanics  
Division of material and computational mechanics  
WRIST  
Chalmers University of Technology  
SE-412 96 Gothenburg  
Telephone +46 31 772 1000

Cover: Thermo-mechanical simulation of a rail after the friction welding process.

Typeset in L<sup>A</sup>T<sub>E</sub>X  
Gothenburg, Sweden 2017

FE modeling of friction welding  
Thermo-mechanical simulations using ABAQUS  
Håkan Ringius  
Clas Thorsell  
Department of applied mechanics  
Chalmers University of Technology

## Abstract

The WRIST project (Innovative Welding Processes for New Rail Infrastructure) aims to develop and present new methods for joining rails. One of the methods proposed is Orbital Friction Welding (OFW) of rails using an intermediate disk. The process is still in development and numerical simulations can provide useful insight and guidance on how to further develop this welding process.

This thesis presents 3D thermo-mechanical modeling of OFW for pearlitic rails and 2D axisymmetric modeling of rotary friction welding of thin-walled pipes. Process parameters and sensitivity to material parameters have been studied for both welding methods.

From the simulations, it is shown that correct modeling of the generated heat, during the frictional motion, is of high importance. Therefore, this report also presents a model framework which can be used for calibrating a heat generation model based on experimental data. This framework is based on the developed 2D axisymmetric model and has been evaluated using several heat generation models. A model based on a piecewise linear variation for the coefficient of friction with respect to temperature is deemed as the most promising of the considered models.

Thermal simulations of OFW for rails have been performed to evaluate the temperature field in the rail and the intermediate disk. Results shows that machine components such as rail clamps have little effect on the resulting temperature field as well as cooling rates. Furthermore, it is shown that a longer heating phase is more likely to result in a pearlitic microstructure in the heat affected zone and is, therefore, preferable.

Mechanical simulations of friction welding leads to severe mesh distortions and consequently numerical issues. The results presented are therefore somewhat limited. However, two methods for overcoming this problem has been identified: remeshing during simulation and introduction of visco-plastic material behavior. Both methods are suggested for further study. Finally, models for yield strength at high temperatures are presented and discussed, a material parameter identified as crucial for accurate simulation of the welding process.

Keywords: Orbital friction welding of rails, Mesh to mesh solution mapping, R260 rail grade steel



## Acknowledgements

We would like to express our gratitude to supervisor Lennart Josefsson and examiner Jim Brouzoulis for their guidance and trust. A special thanks goes out to Ivar Wahlstedt, Roeland Bisschop and Carolyn Oddy who were always forthcoming and had done similar studies which was of aid during the learning process.

We would also like to thank Christer Persson and Johan Ahlström who helped us understand and interpret material behaviour for steel at high temperatures.

Clas Thorsell, Håkan Ringius, Gothenburg, March 2017



# Contents

<b>List of Figures</b>	<b>xi</b>
<b>1 Introduction</b>	<b>1</b>
1.1 Background . . . . .	1
1.1.1 WRIST project . . . . .	1
1.2 Friction welding . . . . .	1
1.2.1 Welding scheme . . . . .	2
1.3 Previous work . . . . .	3
1.4 Purpose and deliverables . . . . .	3
1.5 Delimitations and assumptions . . . . .	3
<b>2 The Governing Equations</b>	<b>5</b>
2.1 Thermal equations . . . . .	5
2.2 Mechanical equations . . . . .	5
<b>3 Modeling of material behaviour</b>	<b>7</b>
3.1 High temperature behaviour of steel . . . . .	7
3.2 Carbon steel micro-structure . . . . .	7
3.2.1 CCT-diagrams . . . . .	8
3.3 Modeling R260 rail grade steel . . . . .	9
3.3.1 Plastic behaviour . . . . .	9
3.3.2 Strain rate dependence . . . . .	11
3.4 Modeling micro-structure phase shifts . . . . .	11
3.5 Modeling of the friction coefficient . . . . .	12
<b>4 2D Axisymmetric Model for Calibration and Evaluation</b>	<b>15</b>
4.1 Geometry and mesh . . . . .	15
4.2 The problem with simulating friction welding . . . . .	16
4.3 The remeshing methodology . . . . .	17
4.3.1 Primary model . . . . .	17
4.3.1.1 Fully coupled thermo-mechanical modeling . . . . .	17
4.3.1.2 Process parameters . . . . .	17
4.3.1.3 Boundary and contact conditions . . . . .	18
4.3.2 Python scripting . . . . .	19
4.3.3 Remesh model . . . . .	19
4.4 Numerical simulation . . . . .	20
4.5 Heat flux models and heat calibration . . . . .	23

4.6	Material model comparison . . . . .	27
<b>5</b>	<b>Orbital Friction Welding of Rails</b>	<b>29</b>
5.1	Model Geometries . . . . .	29
5.1.1	Full model . . . . .	29
5.1.1.1	Thermal sinks: full Model . . . . .	30
5.1.1.2	Rail and disc: full Model . . . . .	31
5.1.2	Simplified geometry . . . . .	32
5.2	Meshes . . . . .	33
5.3	Thermal modeling . . . . .	34
5.3.1	Simulation schemes . . . . .	37
5.4	Mechanical modelling . . . . .	38
<b>6</b>	<b>Thermal and mechanical results from modeling of orbital friction welding</b>	<b>41</b>
6.1	Thermal results . . . . .	41
6.1.1	Specification of nodes used in evaluation . . . . .	42
6.1.2	General results, HAZ, cooling rates . . . . .	44
6.1.3	Effects of rail clamps . . . . .	46
6.1.4	Modeling errors and discrepancies . . . . .	48
6.2	Results Mechanical simulation of the simplified model . . . . .	50
<b>7</b>	<b>Conclusion</b>	<b>53</b>
7.1	Pipe system for evaluation and calibration . . . . .	53
7.1.1	Heat flux modeling . . . . .	53
7.1.2	Material behavior . . . . .	54
7.1.3	Dealing with mesh distortion . . . . .	54
7.2	The Rail system for process evaluation . . . . .	54
7.2.1	Effects of process parameters . . . . .	54
7.2.2	Numerical stability . . . . .	55
<b>8</b>	<b>Future work</b>	<b>57</b>
8.1	Numerical stability . . . . .	57
8.2	Thermal modeling . . . . .	57
	<b>Bibliography</b>	<b>59</b>
<b>A</b>	<b>Remeshing PYTHON script</b>	<b>I</b>
<b>B</b>	<b>Pipe remeshing, Results</b>	<b>VII</b>
<b>C</b>	<b>Pipe remeshing, Results</b>	<b>IX</b>
<b>D</b>	<b>Thermal Results</b>	<b>XI</b>
<b>E</b>	<b>Mesh convergence</b>	<b>XVII</b>
<b>F</b>	<b>Material parameters</b>	<b>XIX</b>

# List of Figures

1.1	Principal sketch orbital friction welding . . . . .	2
1.2	Examples of loading schemes for the welding process . . . . .	2
3.1	CCT-diagram for R260 rail grade steel. . . . .	9
3.2	Different models for the behaviour of the yield strength with respect to temperature . . . . .	10
3.3	Specific heat with the phase shift marked in the image. . . . .	11
3.4	The friction coefficient as calculated from Equation 3.4. . . . .	12
3.5	The friction coefficient from the Tri-linear model as suggested in [1, 3].	12
3.6	Illustration of the friction coefficient using Tau model from equation 3.5 for different values of the pressure. . . . .	13
3.7	Comparison of heat flux models with respect to temperature for sev- eral pressure loads. . . . .	13
4.1	Geometry of the pipe used in the simulations. $\Gamma$ represents the names of the boundaries and P is the pressure that is applied. . . . .	16
4.2	Mesh distortion due to excessively stretching and twisting of the mesh.	16
4.3	The mesh to mesh solution mapping method illustrated as a block diagram assuming that the primary model failed. . . . .	17
4.4	Illustration of the process parameter, pressure. Relative velocity is assumed to be 1 m/s over the heating phase. . . . .	18
4.5	Illustration self interaction due to the flash formations. . . . .	19
4.6	Two-pipes model: Mesh after remeshing. (a): Mesh at Heating phase, time: 0s. (b): Mesh at Heating phase, time: 3 s. (c): Mesh at Forging phase, time: 6 s. (d): Shortening of the pipes during the process. (e): Difference between a thermal model and a thermo-mechanical model at the contact surface. . . . .	20
4.7	Rigid-Plane model: Mesh after remeshing, upper pipe replaced by a rigid plane, this model also used linear elements. (a): Mesh at Heating phase, time: 0s. (b): Mesh at Heating phase, time: 3 s. (c): Mesh at Forging phase, time: 6 s. (d): Shortening of the pipes during the process. (e): Difference between a thermal model and a thermo-mechanical model. . . . .	22
4.8	Example of mapping error on the temperature field in the rigid plane model. . . . .	22
4.9	New geometry that is to be used in the heat calibration experiments.	23
4.10	Maalekians proposed heat flux characteristics [6] . . . . .	23

4.11	Assumed process parameters resembling that of the WRIST calibration test plan [25]. (a): Loading cycle. (b): Relative velocity cycle . . .	24
4.12	Behaviour of the Tri-linear model for different values of the $T(\mu=0)$ . (a): Heat flux. (b): Temperatures. upper image: at contact surface. lower image: 5mm from contact surface. . . . .	24
4.13	Behaviour of the Tri-linear model for different values of the maximum friction coefficients. (a): Heat flux. (b): Temperatures. upper image: at contact surface. lower image: 5mm from contact surface. . . . .	25
4.14	Behaviour of the Tau model for different material models. (a): Heat flux. (b): Temperatures. upper image: at contact surface. lower image: 5 mm from contact surface. . . . .	26
4.15	Behaviour of the Tau model for different values of the $\text{Min } \tau_y$ . (a): Heat flux. (b): Temperatures. upper image: at contact surface. lower image: 5 mm from contact surface. . . . .	26
4.16	The images shows the model change in the Tau model for the given process parameters . . . . .	26
4.17	An example of flash formations during the friction welding process, cf. [26] . . . . .	27
4.18	Rigid-Plane model: loading cycle 1, $P_{\text{Forge}} = 150\text{MPa}$ , Soucal viscoplastic, isotropic hardening model. (a): Flash formations (b): 3D view of the flash formations . . . . .	28
4.19	Rigid-Plane model: Skyttebol kinematic hardening model. $P_{\text{heating}} = 2\text{MPa}$ , $P_{\text{Forge}} = 150\text{MPa}$ (a): Flash formations long load ramping times (b): 3D view of the flash formations Long load ramping times. . . . .	28
5.1	(a) <i>full model</i> . (b) <i>full model</i> symmetry surfaces. . . . .	29
5.2	Clamps. (a) Rail clamp. (b) Specified thickness and width of the rail clamp. (c) Geometry of disc sink. (d) Positions of major clamps . . .	30
5.3	Cylinder sinks. (a) Geometry of cylinder sinks (b) Positions of cylinder sinks . . . . .	31
5.4	Rail geometry. (a) Rail, showing partitions. (b) Rail second view. . .	31
5.5	Disc specification. Figure showing the sections of the disc. . . . .	32
5.6	Simplified Rail model . . . . .	32
5.7	Full mesh shown in figure. . . . .	33
5.8	(a) Rail mesh. (b) Disc mesh. . . . .	33
5.9	Mesh of the simplified rail model . . . . .	34
5.10	Temperature field visualized at the end of heating phase . . . . .	34
5.11	Heat surfaces. (a) Surfaces with applied heat flux. (b) Orbital motion increasing heating surface on disc . . . . .	35
5.12	Contact surfaces. (a) Contact areas on the rail and disc to thermal sinks. (b) Contact area on the rail clamp. (c) Contact surfaces concerning rail to disc. . . . .	36
5.13	Temperature boundary conditions on thermal sinks . . . . .	36

5.14	(a) Process parameters vs time, 20 sec heating phase(T4 and T5). (b) Process parameters vs time, 9 sec heating phase, (T1 to T3). (c) Process parameters vs time, 5 sec heating phase, (M1). (d) $\mu$ vs T( $^{\circ}$ C), trilinear model . . . . .	37
5.15	Figures showing loading surface and loading cycle. (a) Rail loading surface. (b) Loading cycle. . . . .	39
5.16	Figures showing symmetry and contact surfaces. (a) Symmetry sur- faces of simplified model. (b) Contact surfaces of simplified model. . .	39
6.1	Temperature field visualized at the end of heating phase . . . . .	41
6.2	Figures describing system for defining nodes. (a) bL line on Rail. (b) bL line shown in mesh. (c) Closer look at bL line with starting point circulated. (d) Figure of how nodes are defined by their distance to the starting point. . . . .	42
6.3	Specified lines used for evaluation shown as red lines. (a) cL line. (b) nL line . . . . .	43
6.4	dL lines shown in red with starting points circulated . . . . .	43
6.5	HAZ visualized in red for T1 simulation. (a) HAZ on rail and disc, (b) HAZ on x-symmetry surface. . . . .	44
6.6	Graphs showing variations in temperature along bL for simulations T1 and T4 for comparison on the size of the HAZ. (a) Temperature variation along bL for T1, (b) Temperature variation along bL for T4. . . . .	44
6.7	Graphs showing variations in temperature along dL2 for simulations T1 and T4 for comparison on the size of the HAZ. (a) Temperature variation along dL2 for simulation T1 (b) Temperature variation along dL2 for simulation T4. . . . .	45
6.8	(a) CCT diagram comparing cooling rates at 3 different points con- cerning simulation T1. (b) CCT diagram comparing cooling rates between simulations T1 and T4 . . . . .	45
6.9	Evaluation of rail clamp effects. (a) CCT diagram comparing cooling rates at different nodes along cL for simulation T1. (b) Temperature field visualized at end of heating phase demonstrating positions of lines with respect to rail clamp. . . . .	46
6.10	Evaluation of rail clamp effects. (a) Temperature variation along cL for simulation T1 (b) Temperature variation along cL for simulation T4. . . . .	47
6.11	(a) Temperature variation along nL for simulation T4 (b) CCT dia- gram comparing cooling rates at different nodes along nL for simula- tion T4. . . . .	47
6.12	Temperature variation along dL3 for simulation T4. . . . .	49
6.13	Figures demonstrating modeling errors of contact condition and offset heatflux surface (a) The uniform heatflux over the offset implemented in models used. Contact condition implemented effecting heat flux at contact surface while not at offset surface (b) Figure demonstrating how a more accurate model of the heat flux over the offset could be implemented. . . . .	49

6.14	Visualization of total displacement after the forging phase. (a) Full view. (b) Zoom in at railhead. (c) Zoom in at upper rail curvature. (d) Zoom in at lower rail curvature. . . . .	51
6.15	Visualization of total displacement after the forging phase at x-symmetry surface. (a) Full view. (b) Zoom in at railhead symmetry surface. (c) Zoom in at Railfoot symmetry surface. (d) Specified total displacement in figures. . . . .	51
6.16	(a) Axial displacement during heating and forging. (b) Axial displacement during forging . . . . .	52
B.1	2 pipe model: Flash formations when using the mesh to mesh remeshing method . . . . .	VII
C.1	rigid plane model: Flash formations when using the mesh to mesh remeshing method . . . . .	IX
D.1	Time vs temperature, T1, T2, T4 and T5 (with and without sinks) at nodes on cL located 3.33mm and 5mm from the disc. Node located at 5mm from the disc is in contact with the clamp. . . . .	XI
D.2	Results from simulation with sinks for 9 and 25 seconds long heating phase at nodes located on dL3 . . . . .	XII
D.3	Results from simulation with sinks for 25 seconds long heating phase at nodes located on dL3, demonstrating the difference in cooling rate between nodes located at 5 and 7mm from starting point of dL3 . . .	XIII
D.4	Results regarding material evaluation along cL, clamp is located at 5mm . . . . .	XIII
D.5	Figure results from simulations T1 and T2 are presented for nodes along bL with the aim to evaluate the general effect of the rail clamp. a) Temperature variation for nodes along bL to determine size of the HAZ. b) CCT diagram demonstrating the effect on the cooling rate of the rail clamp . . . . .	XIV
D.6	(a) Temperature variation along dL2 for simulation T1 (b) CCT diagram comparing cooling rates at different nodes along dL2 for simulation T1. . . . .	XIV
D.7	CCT diagram comparing cooling rates at different nodes along dL3 for simulation T4. . . . .	XV
E.1	Mesh convergence . . . . .	XVII
F.1	. . . . .	XIX
F.2	. . . . .	XX

# 1

## Introduction

### 1.1 Background

Railways serve as a monument of the industrial era. Even though the technology surrounding railways have been developed for centuries there is room for improvement. Rails have a limited lifetime which is mainly governed by the deterioration at joining intersection between rail. Today rails are most commonly joined through thermite welding, a casting process which involves pyrotechnic fuels and results in an intermediate component joining the rails. One issue concerning this process is that the rail inherits inhomogeneous surface hardness in the area of the connection, in what is referred to as the heat affected zone (HAZ). With the joints being subjected to rolling contact fatigue these zones are worn down unevenly creating bumps and cavities which may lead to several fatigue problems for both rail and wheels. Therefore, minimizing the heat affected zone caused by the joining process is of great importance.

#### 1.1.1 WRIST project

The research project WRIST, funded by the European Union, serves to develop cost effective and flexible joining processes for rail products. Of special interest are processes joining the recently introduced bainitic rail steel grades for which existing processes are inadequate. WRIST focuses on developing two methods namely, automatic forged aluminothermic welding and orbital friction welding whereas this thesis solely considers the latter method (friction welding). The new methods aims to reduce the heat affected zone and minimize the loss of mechanical properties. Orbital friction welding is furthermore environmentally friendly relative commonly used welding processes [11].

### 1.2 Friction welding

Friction welding is a solid state joining process which generates heat through mechanical friction between the joining parts. An axial force is applied which deforms the material and the heated parts are forged together. Friction welding is quick, does not involve the use of consumables and allows the material to retain its original properties relatively well compared to other processes. In this thesis two different

forms of frictional welding are considered, rotary and orbital welding.

Rotary welding, also known as spin welding, keeps one part stationary while the other part rotates at high speeds and is then pressed against the stationary part. This process will generate an inhomogeneous heat flux, since the relative velocity between the components vary linearly over the radius. However for thin walled tubes the flux can be considered uniform.

To induce a uniform heat flux orbital friction welding (OFW) is used. OFW applied to joining rails involves a disc which moves in a small orbit, see Figure 1.1. Performed correctly this will induce a uniform velocity profile over the contact surface.

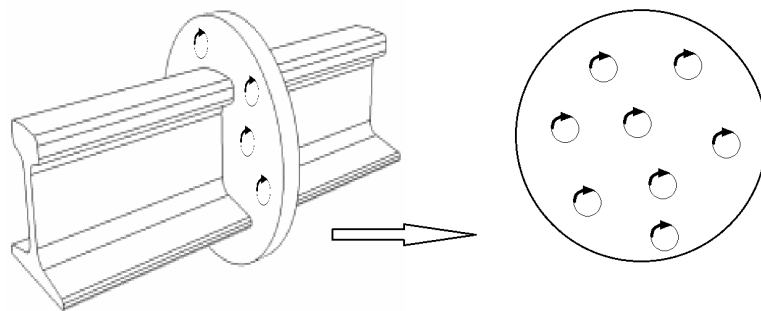


**Figure 1.1:** Principal sketch orbital friction welding

### 1.2.1 Welding scheme

The welding process consists of three steps; Heating, Forging and Cooling. In the heating step the parts move relative to each other while a load is applied resulting in a heat flux. This relative velocity is assumed to be constant over the interaction surface. In the Forging step a load is applied pressing the pieces together. The load is then released for the cooling phase, where the joined piece is allowed to rest. This loading scheme is illustrated in Figure 1.2. There are several suggestions on the time, pressure and time parameters in the pictures and these parameters varies strongly between sources.

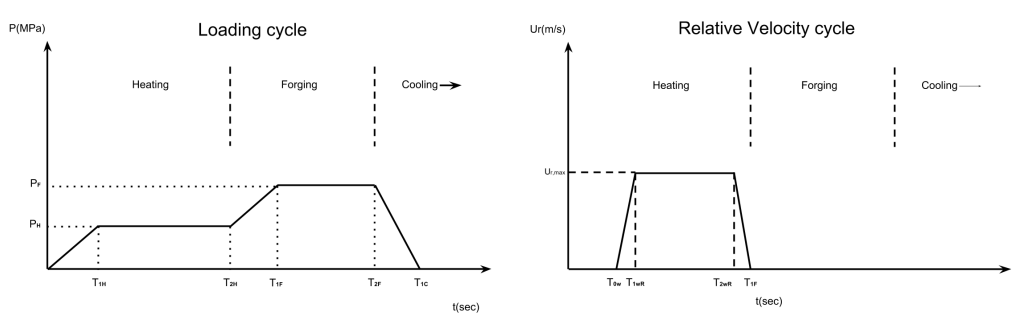


**Figure 1.2:** Examples of loading schemes for the welding process

### 1.3 Previous work

In [5], Maalekian et.al simulated orbital friction welding on a square bar in which he divided up the problem and solved for a thermal and a mechanical simulation. His work found that the method yielded a small HAZ concluding that the joining method could prove effective.

During spring of 2016 two projects were performed at Chalmers concerning orbital welding by I. Wahlstedt and R. Bisschop et.al in [1] respectively [2]. Both studies investigated orbital welding of a beam with an orbiting plate between the bars. The methods used to solve the problem closely resemble one and another as both use the methodology presented by Maalekian.

As [1,2,5] uses different processing parameters they are not directly comparable to each other, but it is worth noting that both [1] and [2] simulations resulted in a significantly larger HAZ than [5].

During the summer of 2016 R. Bisschop and C. Oddy studied possible improvements of the results from [1,2] in [3,4]. They evaluated the existing heat model, contact conditions, meshing, mesh types and more.

Other related studies made on thermo-mechanical rotational friction welding simulations are presented in [16,20–22]. All of these studies deals with so called super-alloy pipes and three of them managed to simulate the complete friction welding processes using remeshing based on deformed geometries. Soucal et.al in [16] whom was not able to simulate the complete process was able to simulate about 1 millimeter axial shortening.

### 1.4 Purpose and deliverables

The aim of this master thesis is to develop a thermo-mechanical FE-model for OFW of rails. Effects of different process parameter will be studied along with mesh sensitivity and numerical stability. A alternative methodology for simulation of friction welding will also be presented.

The project aims to deliver the following:

- Axisymmetric model to be used for calibration of a heat generation model
- Axisymmetric model to be used for validation of material model
- Alternative simulation methodology
- Thermal simulation and analysis off rail geometry
- Thermal evaluation concerning sensitivity to geometrical changes
- Mechanical simulation and analysis off rail geometry
- A thesis report

### 1.5 Delimitations and assumptions

No experimental evaluation will be done for the simulations. Experimental data was expected to be delivered by project partner WRIST during the span of the

## 1. Introduction

---

project. However, due to technical difficulties, this data could not be delivered. Therefore, process and material properties could not be calibrated to the data, limiting evaluation to literature studies.

Material parameters regarding specific heat and thermal conductivity provided by WRIST are assumed to correct and are not evaluated.

# 2

## The Governing Equations

In this section the foundations of the work are presented such as what governing equations that needs to be solved and how some of the system dependencies are mathematically represented.

### 2.1 Thermal equations

Friction welding generate heat through friction and plastic deformations. This energy transport can be modeled based on conservation of energy resulting in equation 2.1.

$$\rho C_p \frac{\partial T}{\partial t} = \nabla^T k \nabla T + \dot{S} \quad (2.1)$$

$\dot{S}$  is the heat generation due to plastic deformation which is assumed to be much smaller than the heat generation through frictional motion. The Heat capacity ( $C_p$ ) and the thermal conductivity ( $k$ ) are both temperature dependent parameters.

Heat generation due to friction is modeled as a heat flux boundary condition.

$$\mathbf{q}(t) = -k \nabla T \quad (2.2)$$

Modeling this heat flux is of great importance in order to get accurate results. The heat flux is chosen to be modeled with the simple friction law  $q = \mu U P$ , were  $U$  as the local relative velocity and  $P$  as the pressure. The friction coefficient ( $\mu$ ) is an unknown and temperature dependent parameter that need to be modeled.

### 2.2 Mechanical equations

The model is considered static and linear isotropic elastic up until yielding. Essentially the balance of momentum equation will be solved in the entire domain, equation 2.3 where  $\rho$  is density and  $\mathbf{f}$  is the body force.

$$\int_{\Omega} \text{div}(\sigma) - \rho * \mathbf{f} d\Omega = 0 \quad (2.3)$$

The stress,  $\sigma$ , in a material depend on the strain,  $\epsilon$ , and they are connected through the constitutive matrix  $\mathbf{D}$ . For the 3D case a  $\mathbf{D}$  matrix is constructed dependent on the type of strain formulation that is used with Young's modulus and poisson's ratio,  $\nu$ .

## 2. The Governing Equations

---

$$\sigma = \mathbf{D} : \epsilon \quad (2.4)$$

For an elastic solid this relation can in tensor notation be written:

$$\sigma_{ij} = \lambda \delta_{ij} \epsilon_{kk} + \mu 2\epsilon_{ij} \quad (2.5)$$

Where

$$\lambda = \frac{E\nu}{(1-2\nu)(1+\nu)}, \mu = G = \frac{E}{2(1+\nu)} \quad (2.6)$$

It is common and very practical for computational purposes to divide the strain in a volumetric  $\epsilon^v$  and deviatoric  $\epsilon^{dev}$  part.

$$\epsilon_{ij}^v = \delta_{ij} |\epsilon_{kk}|, \epsilon_{ij}^{dev} = \epsilon_{ij} - \epsilon_{ij}^v \quad (2.7)$$

Dealing with plastic deformations and thermal expansion this formulation is convenient and the constitutive model for the stress is expressed in the following manner.

$$\sigma_{ij} = 2G(T, \epsilon_{ij}^{dev}) \epsilon_{ij}^{dev} + K(T) \epsilon_{ij}^v(T) I_{ij} = D^{el}(T, \epsilon_{ij}^{dev}) : \epsilon(T) \quad (2.8)$$

The von Mises yield criterion will be used to model the plastic deformation. With this criterion the material will behave elastic upon passing the yield stress. Solely the deviatoric stress is used to determine if the material has reached the point of yielding. Using the yield function, equation 2.9, stating that the yield function has to be equal to or less than zero.

$$\phi = \sqrt{3/2} |\sigma_{ij}^{dev}| - \sigma_y, \sigma_{ij}^{dev} = \sigma_{ij} - \delta_{ij} |\sigma_{kk}| \quad (2.9)$$

# 3

## Modeling of material behaviour

In order to solve the governing equations from Section 2 the material properties needs to be defined. The material in question is a R260 rail grade steel. However, as the friction welding process for R260 is in such an early stage of development there are many unknowns. This section describes the behaviour of metals and how this is implemented for the R260 rail grade material model.

### 3.1 High temperature behaviour of steel

As metals approaches their melting temperature they lose their hardening behaviour and transitions into a more visco-plastic behaviour. It is uncertain when and how quickly this transition takes place but the material is assumed to have reached a purely visco-plastic behaviour at 70 % of the melting point as suggested by Gantchenko et al. in [23].

At the time of this study the behaviour of R260 rail grade is unknown for temperatures above 600 °C and no suitable material model could be found that includes visco-plastic behaviour. Theoretical behaviour of high temperature metals will therefore be used in order to understand the high temperatures effects on the R260 rail grade.

The friction welding process is a solid state method, meaning that the material will be less then the melting temperature of about 1470 °C for the studied R260 rail grade. Note however, the material will experience temperatures up to 1200 °C, making the visco-plastic behaviour of the material relevant.

During the friction welding process the material will experience extremely large strains, strain rates and temperatures. These conditions will cause the material to behave in an incompressible manner near the contact surface cf. [20, 22]. In [22], L. D'Alvise et al. claim that it is this visco-plastic incompressible behaviour that create the flash formations and governs their shape.

### 3.2 Carbon steel micro-structure

Carbon steel consists of a crystalline micro-structure where the grain size and composition strongly effect the material properties. The crystalline nature is divided into so called material phases which consists of: ferrite, cementite, pearlite, bainite and martensite. Pearlite and bainite is a mix of ferrite and cementite. In pearlite

the ferrite and cementite has formed a layered structure while the bainite has a ferrite plate structure surrounded with cementite. Martensite is similar to bainite having a ferrite plate structure but due to rapid cooling the surrounding cementite does not form. Pearlite is a softer more flexible steel while martensite is a hard, stiff and brittle. Martensite is undesirable in the weld since homogeneous material parameters are sought for.

The R260 rail grade steel is a pearlitic steel but if it is heated to above approximately  $730\text{ }^{\circ}\text{C}$  it starts changing phase to austenite. The phase change is not instant at a certain temperature (as for the case of ice to water) but instead changes at different rates dependent on the temperature. For these short time spans of heating, determining exact volume fractions of austenite has been set aside. It is instead assumed in this project that a significant amount have been transformed to austenite if the temperature has reached  $800\text{ }^{\circ}\text{C}$  or above. If any part of the rail or disc reaches this temperature they are considered to be in the heat affected zone, (HAZ). What phase the material in the HAZ ends up having is determined by the cooling rate and this is typically analysed using a Continuous Cooling Transformation diagram (CCT diagram) seen in Figure 3.1.

#### 3.2.1 CCT-diagrams

This section describes how CCT-diagrams are used and interpreted. Understanding how to interpret these diagrams is of great importance as they are used to present a large portion of the results later in the report. The CCT diagram is used in the following manner to determine the microstructure. There are 4 lines concerning start and end of transformation shown in the diagram, see Figure 3.1. P1 is for pearlite and B1 is for bainite, these indicate start of transformation. If the cooling rate is fast enough for the curve not to cross the starting lines no austenite will have transformed into either pearlite or bainite. In that case all will have transformed to martensite.

P2 and B2 indicate end of transformation corresponding to 100% transformation. If austenite is cooled from  $860\text{ }^{\circ}\text{C}$  to approximately  $500\text{ }^{\circ}\text{C}$  in more than 100 seconds the cooling process will have transformed to 100 % pearlite. The temperature against time curve will then have crossed the green pearlitic line meaning that all austenite have transformed to pearlite. This is preferable since R260 Rail grade steel is a pearlitic steel.

For cooling rates corresponding to less than 100 % volume fractions are approximated by fractions of length where the cooling curve intersects the dotted line. Has an example, if the cooling rate from austenisation temperature is  $10\text{ }^{\circ}\text{C}/\text{s}$  the austenite will first have transformed to approximately 80 % pearlite. This is approximated by studying where the curve crosses the dotted line concerning pearlite transformation. The remaining austenite, (20 %), is transformed to approximately 40 % bainite and 60 % martensite by studying where the curve crosses the dotted line for bainite transformation. Volume fractions of pearlite, bainite and martensite would then be 80 %, 8 % and 12 % respectively.

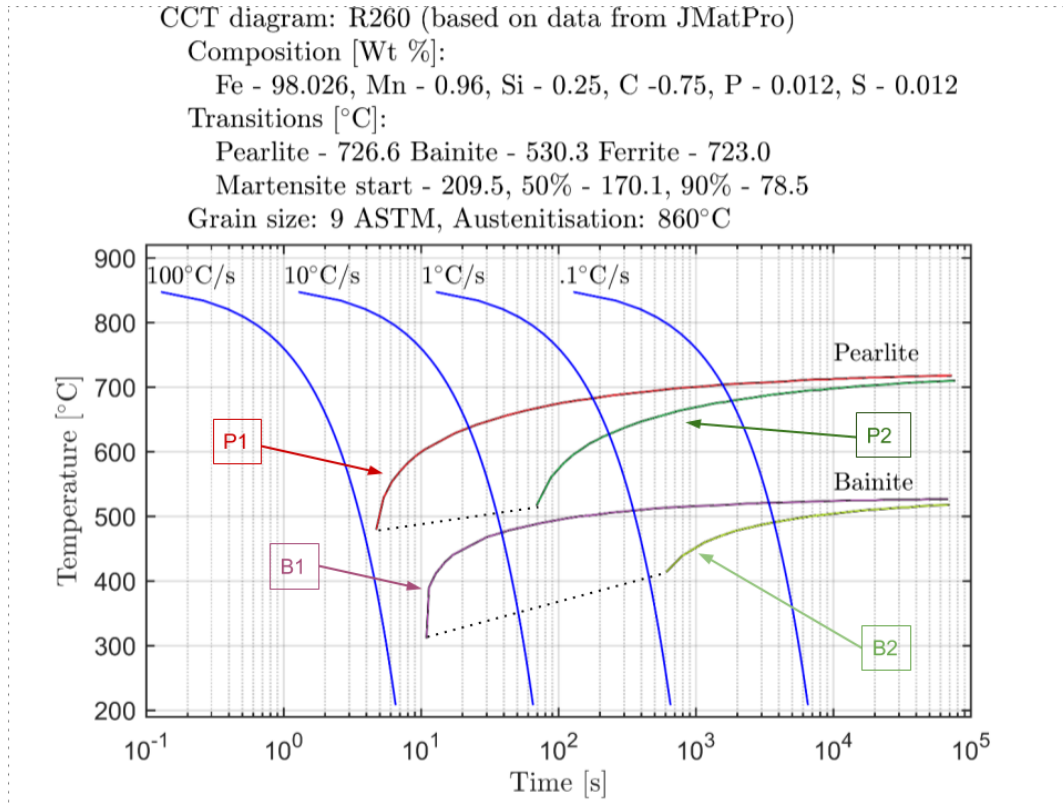


Figure 3.1: CCT-diagram for R260 rail grade steel.

### 3.3 Modeling R260 rail grade steel

For the friction welding process the rail experiences high loads together with high temperatures. The model therefore needs to include Young's modulus, Poisson's ratio, yield strength, hardening parameters, specific heat, heat conductivity, annealing temperature and thermal expansion.

These parameters are partially provided by WRIST cf. [11] and complemented with material parameters from Chen et al. cf. [14] and Skyttebol et al. cf. [13]. The model is implemented into ABAQUS<sup>1</sup> as data points which ABAQUS linearly interpolates between.

#### 3.3.1 Plastic behaviour

In [13], Skyttebol presented a plasticity model with linear kinematic hardening for two data points at 20 °C and 600 °C. A third point was estimated to be  $\sigma_y(T = 1000) = 10$  MPa. The first two points were obtained through experimental testing and will therefore be considered the most reliable data available. Between the data points the yield strength is assumed to vary linearly and this model will be referred to as the *Skyttebol model* in this thesis. This model was used, with some variations, in previous studies such as [1–4] which studied modeling aspects of OFW using the R260 rail grade steel.

<sup>1</sup>ABAQUS® Dassault Systèmes, release 6.13

Since the yield strength is unknown between the three data points and unlikely to vary linearly in between points as in the Skyttebol model some general behaviour of steel, cf. [15] and general metal behaviour, cf. [16], could be incorporated in order to improve the model. In Figure 3.2 several models for the yield strength as a function of temperature are depicted. Only yield strength behavior will be used from these sources and is implemented as a reduction factor ( $f_{red}$ ):

$$\sigma_y^{\text{model}}(T) = \sigma_y^{\text{ref}}(T = 20) \cdot f_{red} \quad (3.1)$$

The first suggested model is the Euro code 3, referred to as the *EC3 model*, which is a standardised material behaviour model for structural steel, cf. [15]. The *EC3 model* describes the behaviour up to 1100 °C and suggest that the yield strength goes to zero at 1200 °C. For numerical stability this last point is ignored and replaced with  $\sigma_y(T = 1470) = 5$  MPa. For EC3  $f_{red}$  is defined in [15].

The second suggested model combines the second data point from the Skyttebol data with the behaviour of EC3 for low to intermediate temperatures (less than 800°C). For high temperatures (more than 800 °C) the yield strength model use yield strength behaviour of Astroloy from [17] which is calculated using Equation 3.2. Astroloy is a super-alloy and has been used in several studies of friction welding such as [16, 17]. This model will be referred to as the *Soucail model* and what is worth mentioning about this model predicts a significantly lower yield strength at high temperatures than any of the other models, e.g  $\sigma_y = 0.01$  Pa at 1470 °C.

$$f_{red} = \left( \frac{\sigma_y(T)}{\sigma_y(T = 20)} \right)_{\text{reduction factor}} \quad (3.2)$$

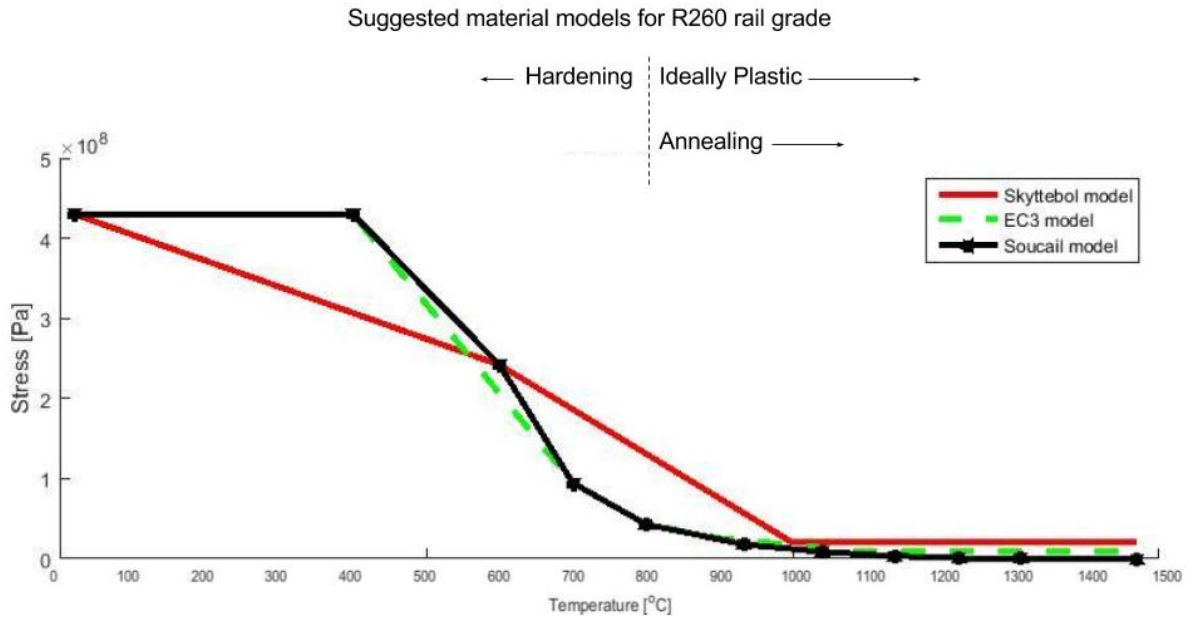


**Figure 3.2:** Different models for the behaviour of the yield strength with respect to temperature

### 3.3.2 Strain rate dependence

As the increasing temperature softens the material visco-plastic behaviour becomes more important. Visco-plastic effects are also important to implement as to ensure numerical stability when using a model, such as the *Soucal model*, which allows the material to soften as far as  $\sigma_{y,\min} = 0.01$  Pa at 1470 °C. As the large strain increments that occur with low yield strength models typically cause the solution to diverge.

The visco-plastic behaviour is also unknown for R260 rail grade. Therefore, another reduction factor is implemented as shown in equation 3.3. This reduction factor is calculated using the data from [17] which uses the same material as Soucal in [16].

$$\sigma_y^{\text{model}}(\dot{\epsilon}, T) = \sigma_y^{\text{ref}}(\dot{\epsilon} = 0, T) \cdot \left( \frac{\sigma_y(\dot{\epsilon}, T)}{\sigma_y(\dot{\epsilon} = 0, T)} \right)_{\text{reduction factor}} \quad (3.3)$$

The strain rate dependence is defined for low,  $\dot{\epsilon} = 0.01 \frac{1}{s}$ , and high,  $\dot{\epsilon} = 50 \frac{1}{s}$ , strain rates with an addition of  $\dot{\epsilon} = 1000000 \frac{1}{s}$  for extreme strain rates in order to avoid divergence when load is increased rapidly.

### 3.4 Modeling micro-structure phase shifts

Chen et.al presented in [14] a model for the behavior of steel micro-structure phase shifts. This model was based on a delayed energy principle where the specific heat is increased during the phase shift, see Figure 3.3. The annealing temperature is estimated to occur at about 800 °C based on phase transformation theory in section 3.2.

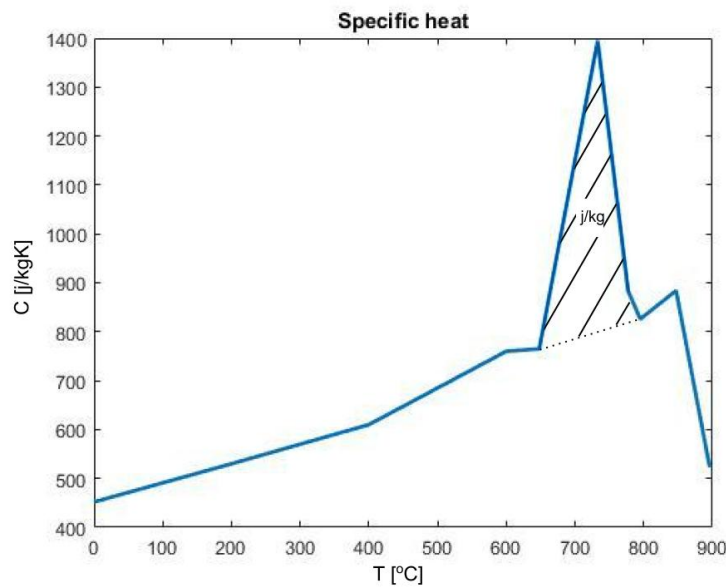


**Figure 3.3:** Specific heat with the phase shift marked in the image.

### 3.5 Modeling of the friction coefficient

In order to define the heat flux in Section 2.1 the coefficient  $\mu$  need to be modeled.  $\mu$  is a complex parameter which is dependent on the rotation speed, temperature and applied load, cf. [24]. In [7], the friction coefficient is suggested to behave as in Figure 3.4. This behaviour is expressed using Equation 3.4:

$$\mu(T) = 0.288 \cdot T^{0.38} e^{-0.002 \cdot T} \quad (3.4)$$

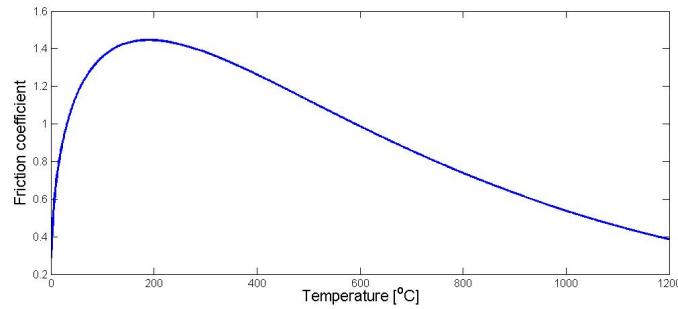


**Figure 3.4:** The friction coefficient as calculated from Equation 3.4.

Using this shape as a initial guess for the friction coefficient, an approximation can be created using three linear sections with respect to the temperature. This model will be referred to as the *Tri-linear model* and is illustrated in Figure 3.5.

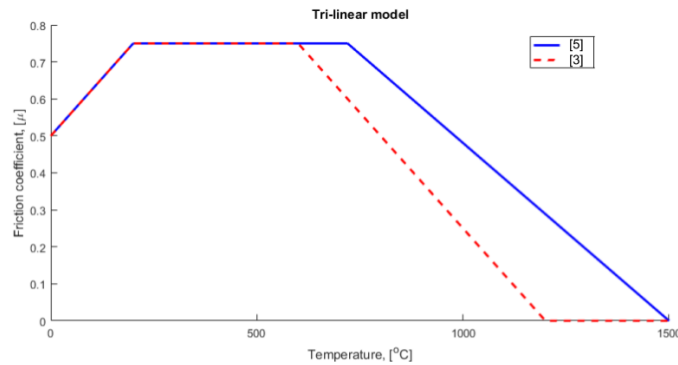


**Figure 3.5:** The friction coefficient from the Tri-linear model as suggested in [1, 3].

An alternative to the Tri-linear model is to use a more theoretical model which is based on the von Mises flow rule criterion for pure shear stress cf. [6]. Through this criterion the friction coefficient becomes pressure dependent which as previously mentioned  $\mu$  is expected to be. This model will be referred to as *Tau-model* and it assumes that the shear stress can never be larger than the yield stress in pure shear. In Figure 4.16, Equation 3.5 is illustrated for different values of the pressure.

$$\mu p = \tau < \tau_y = \frac{\sigma_y}{\sqrt{3}} \Rightarrow \mu = \frac{\sigma_y}{\sqrt{3}p} \quad (3.5)$$

Where  $\tau$  is the shear stress and  $\sigma_y$  is the yield strength.

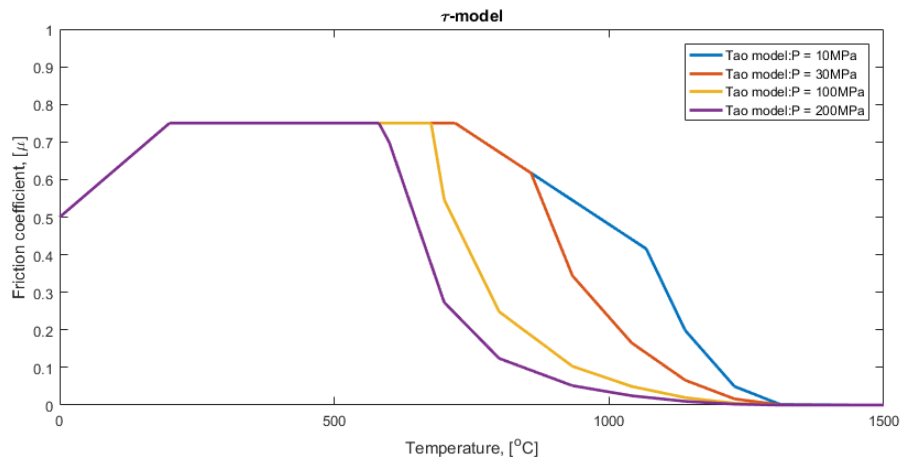


**Figure 3.6:** Illustration of the friction coefficient using Tau model from equation 3.5 for different values of the pressure.

Since the heat flux has been defined as  $q = \mu p v$  in Section 2.1 the Tri-linear model and the Tau model results in heat fluxes as shown in Figure 3.7.

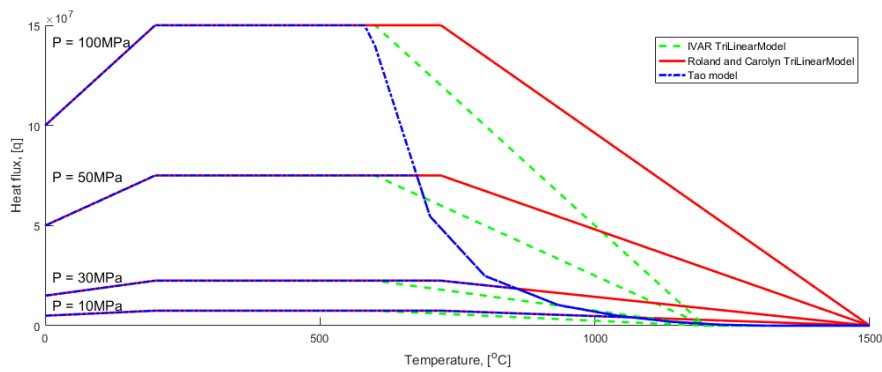


**Figure 3.7:** Comparison of heat flux models with respect to temperature for several pressure loads.



# 4

## 2D Axisymmetric Model for Calibration and Evaluation

In Section 3 there is a large amount of uncertainty among the material data and heat flux models. Such as how to model the yield strength and how to model and calibrate the friction coefficient  $\mu$ . This section will evaluate current models and present how to use mesh to mesh solution mapping in order to remesh a model based on its currently deformed geometry. This will be analysed using rotational friction welding which is described in Section 1.2.

### 4.1 Geometry and mesh

The problem to be solved is a rotational friction welding problem between two pipes that are to be welded together, see Figure 4.1. In order to reduce the computational cost axisymmetry is used, reducing it to a 2D problem, see figure 4.1.

The pipe model is divided into two sub-sections, one close to the welding surface and one that is considered far away from the welding section. In the far away section the fluctuations are considered to be small and therefore a larger mesh is deemed to be satisfactory. Since the model changes with each remeshing the partition is kept at the same distance from the welding surface. This is done using a Datum plane and partition face in the ABAQUS Assembly module.

The geometry is meshed using a free, quad mesh as triangular elements are not supported for this remeshing method. The elements used are 8-node axisymmetric thermally coupled quadrilateral, biquadratic displacement, bilinear temperature, hybrid and linear pressure with reduced integration. As the pipes are expected to experience large deformations at high temperatures the material can be expected to behave in an incompressible manner as mentioned in Section 3.1, for more information see ABAQUS theory [18] or the studies in [20–22]. Due to this the ABAQUS hybrid formulation is therefore chosen as recommended by the ABAQUS manual.

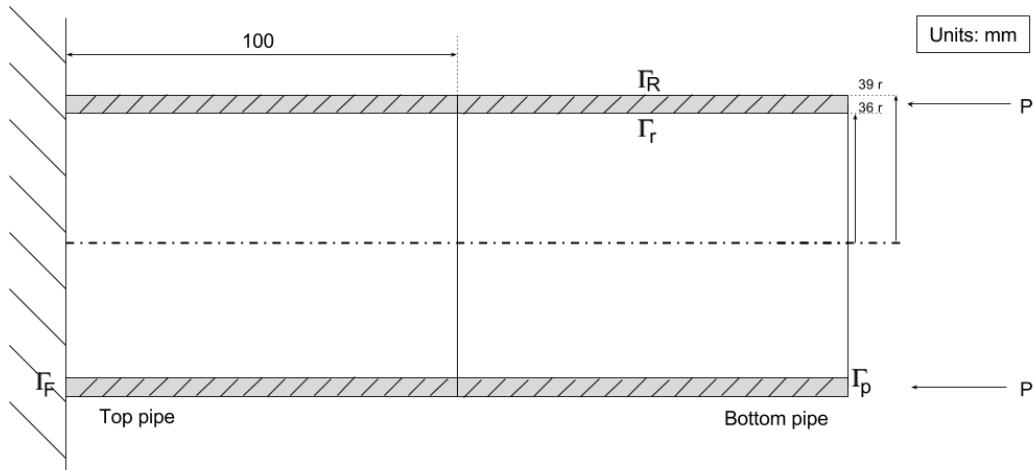


**Figure 4.1:** Geometry of the pipe used in the simulations.  $\Gamma$  represents the names of the boundaries and  $P$  is the pressure that is applied.

## 4.2 The problem with simulating friction welding

During the friction welding process large deformations are expected to occur at the contact surfaces. These deformations are the so-called flash formations and they are the cause of the inherit issue that occur in friction welding simulations. If the flash formations are not accounted for in the simulation model the mesh will become stretched and twisted, leading to numerical inaccuracy and ultimately solution divergence as shown in Figure 4.2.

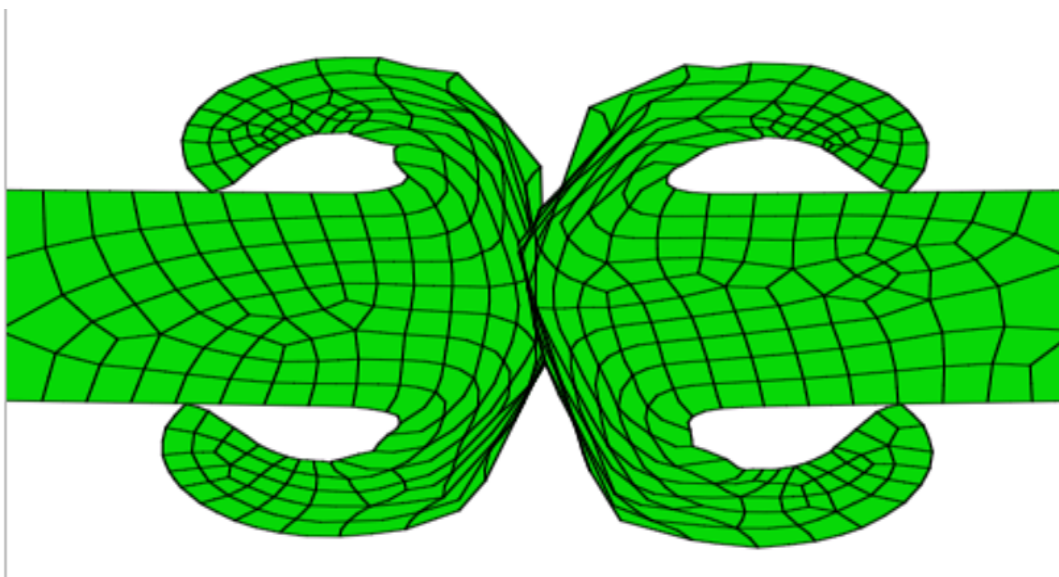


**Figure 4.2:** Mesh distortion due to excessively stretching and twisting of the mesh.

### 4.3 The remeshing methodology

In order to deal with the mesh distortion described in Section 4.2 an alternative methodology using mesh to mesh solution mapping is suggested. The principle of mesh to mesh solution mapping is to run an initial simulation until the mesh distortion becomes unacceptable. At this point the node values is exported and a new geometry is created from the out-lining nodes. For this new geometry a mesh is created and the old nodal values is mapped onto the new mesh. This remeshing process can then be repeated until the loading cycle is completed. The methodology is depicted as a block diagram in Figure 4.3 where alpha is the feature angle which is described in ABAQUS manual cf. [8].

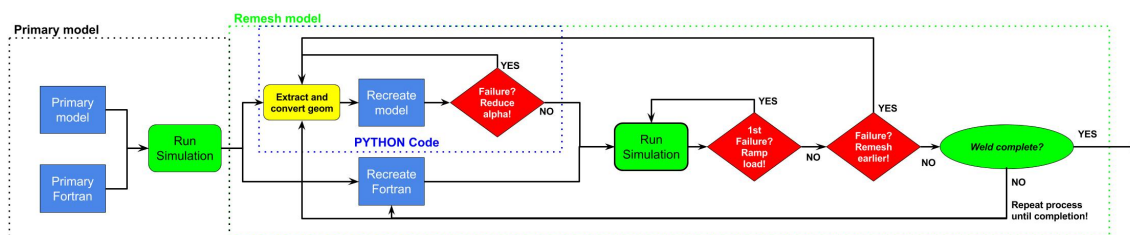


**Figure 4.3:** The mesh to mesh solution mapping method illustrated as a block diagram assuming that the primary model failed.

#### 4.3.1 Primary model

The primary model is the initial model that one start the simulation process from. This simulation model stands as base in recreating the remesh models. The material that is used in this simulation model is the *Soucal model* combined with visco-plastic behaviour as described in section 3.3.2, for a detailed material table see Appendix F.

##### 4.3.1.1 Fully coupled thermo-mechanical modeling

For this remeshing method to work it has to be solved as a coupled system. Whether the solutions are solved separately or together does not matter as the node placements will be associated with the deformations of the mesh. In an uncoupled problem the temperature data will not be associated with the node displacements in the geometry and will therefore not map properly. The fully coupled system is solved using a full newton solver with parabolic extrapolations.

##### 4.3.1.2 Process parameters

The friction welding process parameters can follow most loading cycles, as long as the model is numerically stable enough. There may be convergence issues between the remeshing steps which can be solved by allowing the load to restart from zero and then rapidly rise to its previous value before continuing the loading cycle. The

angular velocity is assumed to have no acceleration time and is instead instantly applied over the heating phase then instantly removed. The loading cycle is illustrated in Figure 4.4.

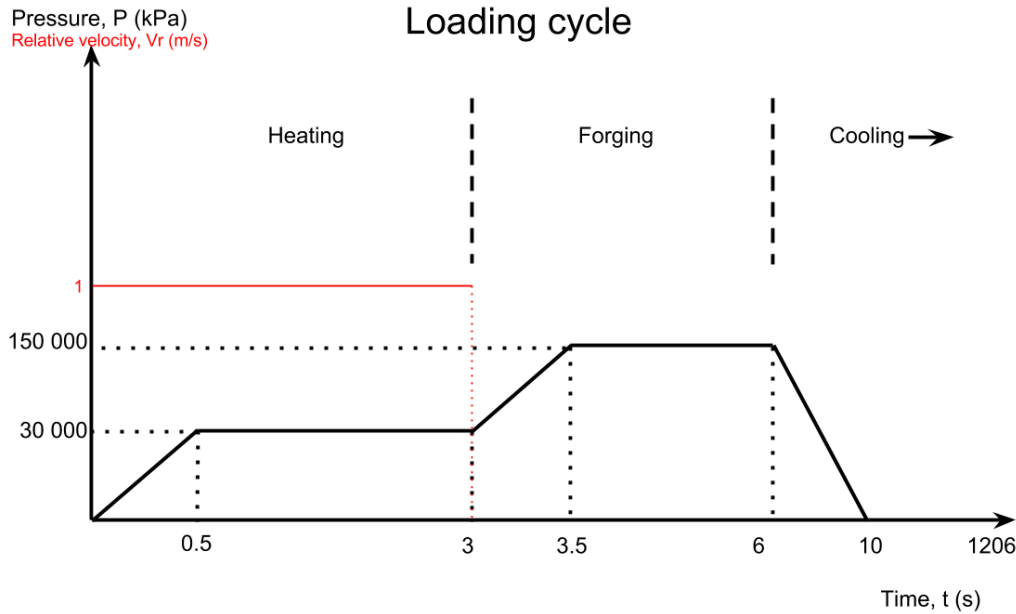


**Figure 4.4:** Illustration of the process parameter, pressure. Relative velocity is assumed to be 1 m/s over the heating phase.

### 4.3.1.3 Boundary and contact conditions

On the bottom pipe the boundary conditions are used in order to prevent free body movements. A *encastre* condition is applied at the top of the top pipe.

Three contact conditions are used. One that expresses the interactions between the two pipes, which is considered to have a frictionless tangential contact, thermal condition assuming perfect conductivity and a *HARD* normal contact (for more information see [8]) which allows separation.

During the process the flash formations are expected to be come in contact with the pipe body see Figure 4.5.

The second contact condition describes the self interaction seen in Figure 4.5. This is important as self intersection is not allowed since it would result in merging of the sections. A surface-to-node self contact conditions is used with a frictionless tangential behaviour and in order to avoid self intersection a tabular normal behaviour is implemented. The tabular normal behaviour expresses the closest self interaction that will be allowed and is chosen as an arbitrarily small value of 0.01 mm. This condition is then reinforced with a arbitrarily large pressure condition of 10 GPa. A thermal condition could be added in order to allow the flash formations to transfer heat during self contact but this was not implemented.

The last contact condition is a surface film condition which covers the faces of

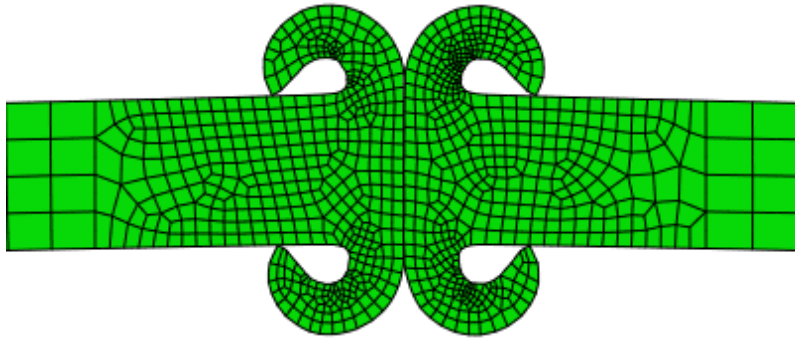


**Figure 4.5:** Illustration self interaction due to the flash formations.

the pipe that are in contact with air,  $\Gamma_R$  and  $\Gamma_r$ , and expresses how quickly heat is transferred to the environment. This is defined with a film coefficient of 6.8 with a sink temperature of 20 °C as suggested by Wahlstedt in [1].

### 4.3.2 Python scripting

The Mesh to mesh solution mapping is a labor intensive method that requires the user to

- Setup the primary model
- Run the primary model
- Extract the deformed mesh at a given increment as a orphan mesh
- Convert the orphan mesh to a geometry
- Recreate the model for the new geometry
- Map solution to the new mesh
- Run the Remeshed model
- Iterate remeshing until the loading cycle is finished

This process can be done using the programming language PYTHON. The most important parts of the script is the two ABAQUS commands *PartFromOdb*, which exports the mesh at a given step as a orphan mesh, and *Part2DGeomFrom2DMesh*, which converts the orphan mesh to a geometry.

The remaining of the script recreate the model and adds a couple of keywords to the model in the end such as:

- \*map solution
- \*controls,analysis=discontinuous

### 4.3.3 Remesh model

Using the current script a large part of the model is possible to recreate, but it is incomplete. There are several steps that needs to be taken to complete the model. Surfaces and sets needs to be reassigned, the keyword *\*MAP SOLUTION* needs to be assigned the remesh step and increment. There is also the issue where the mesh intersects with another body. This might need to be corrected in order to run the simulation.

## 4.4 Numerical simulation

Using the remeshing methodology to simulate friction welding for a axisymmetric problem one can expect the result to resemble those in Figure 4.6 or appendix C, with a displacement curve similar to Figure 4.6d.

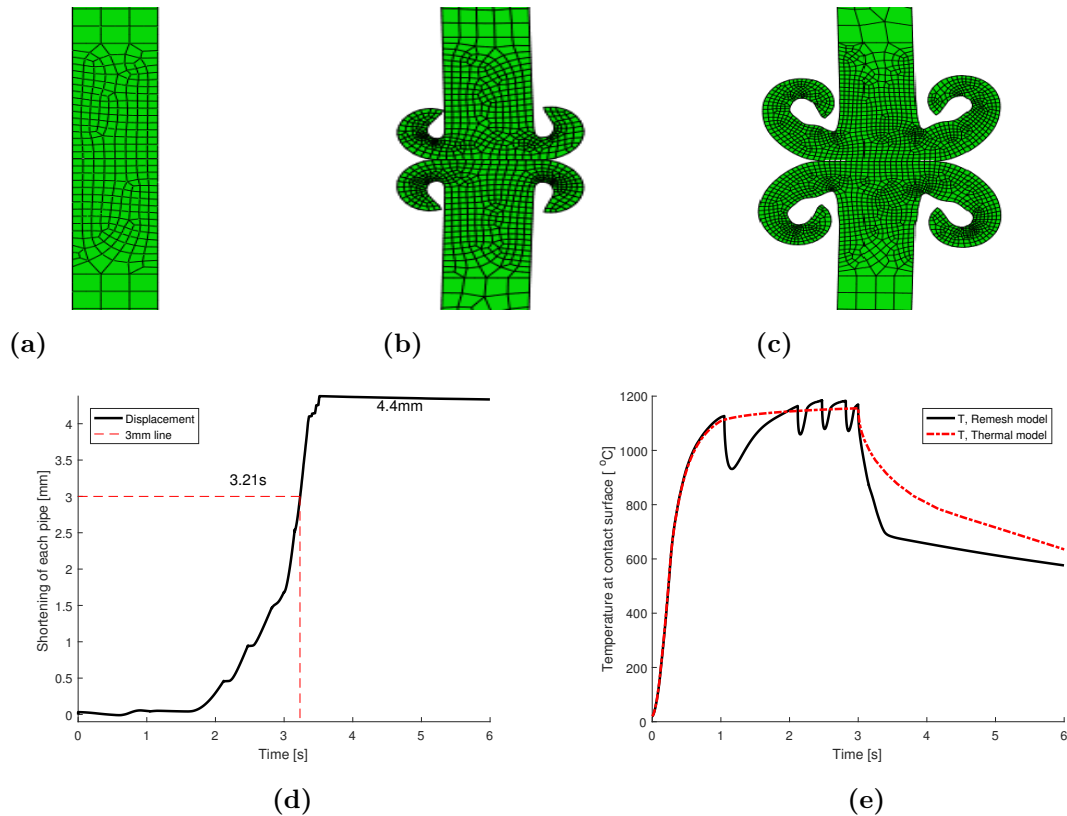


**Figure 4.6:** Two-pipes model: Mesh after remeshing. (a): Mesh at Heating phase, time: 0s. (b): Mesh at Heating phase, time: 3 s. (c): Mesh at Forging phase, time: 6 s. (d): Shortening of the pipes during the process. (e): Difference between a thermal model and a thermo-mechanical model at the contact surface.

In Figure 4.6d one can see mistakes that were made during the process, as for example: the the jagged nature of the displacement curve. This is an effect of overestimating the sensitivity of the remeshed models. The load was gradually reapplied over 0.1 seconds which was far more than was needed. This mistake was corrected on the remeshings in the end of the process reducing the reload time to 0.001 seconds. In the end of the forging load ramp it does not go smoothly to its maximum displacement value. Instead it jaggedly increases due to the instability of the model.

As the method is labour intensive, it may not be reasonable to iteratively calibrate a heat model with the remeshing methodology. It may therefore be necessary to simplify the model to a regular thermal simulation. In figure 4.6e one can see the difference between the temperature at the contact surface in the thermo-mechanical model and the thermal model.

As one can see in figure 4.6e there are some distinct temperature bumps in the Thermo-mechanical line at the start of each remeshing. This is not something that occurs in the thermal simulation. The original suspicion was that the remeshing method caused this drop due to poor mapping. The heat flux was therefore increased in order to compensate for the lost heat, which resulted in the smaller drops and higher max temperatures. With the simulation finished, the loss of heat was calculated over the weld section resulting in a heat loss of 1 % and can not explain the large temperature dips after remeshing.

$$Error = \frac{\int_{\Omega} T_{After} dA - \int_{\Omega} T_{Before} dA}{\int_{\Omega} T_{After} dA} \quad (4.1)$$

The dips are in fact caused by an execution error in the heat flux FORTRAN code and not an issue with the model or method. The load was accidentally made dependent on the local model time instead of being dependent on the global process time which caused the initial ramping load to be applied at the start of each remesh model.

In the forging phase in figure 4.6e one can see that here the temperature drastically deviates from the Thermal results. This is due to that the hottest material is being pushed out into the flash formations. When the flash formations are fully formed the heat flows back into the main piece as the deformations stop.

Simplifying the model by replacing the upper pipe with rigid plane and changing to linear elements gives the result shown in figure 4.7. The appearance of the flash-formations differ between 4.7d and 4.6d, this is most likely caused by the difference of how the loads were applied. The more unstable the model the slower the loads were applied. It is uncertain if the difference of appearance is connected with the change to linear elements. However, considering that the appearance of the flash formations are identical up until the forging phase this could be considered unlikely, to see the whole remesh process see appendix C.

As the rigid planes nodes are locked in space it results in a numerically easier contact condition and the model becomes more stable than the previous two-pipe model. As can be seen in figure 4.7d and 4.7e the curves are not as smooth as one would expect. In contrast to the two-pipes model whose main weakness was model instability, the rigid-plane model weakness are mainly caused by the remeshing methodology. The temperature drops seen in figure 4.7e are caused by mapping errors at the contact surface, as shown in figure 4.8. The overall effect on the temperature field is small but it effects the stability of the model as well as causing a delay in the displacements as the surface stiffens at the start of a remeshed model. This mapping error did not occur when using the two-pipes model.

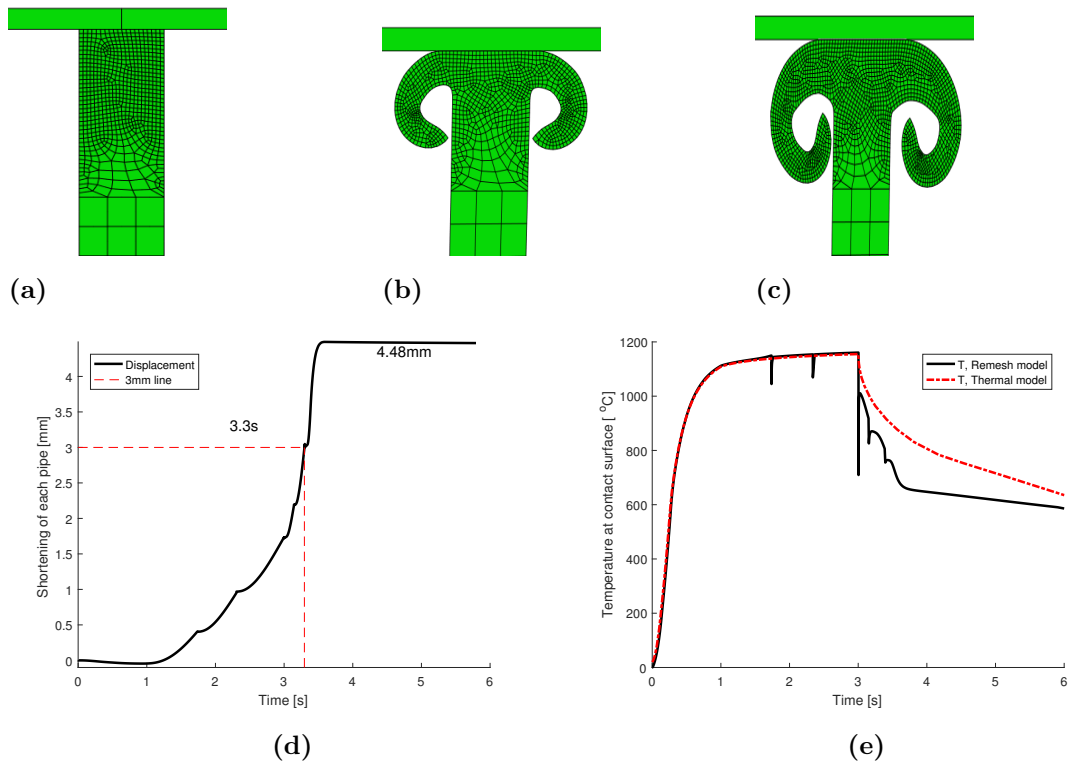


**Figure 4.7:** Rigid-Plane model: Mesh after remeshing, upper pipe replaced by a rigid plane, this model also used linear elements. (a): Mesh at Heating phase, time: 0s. (b): Mesh at Heating phase, time: 3 s. (c): Mesh at Forging phase, time: 6 s. (d): Shortening of the pipes during the process. (e): Difference between a thermal model and a thermo-mechanical model.

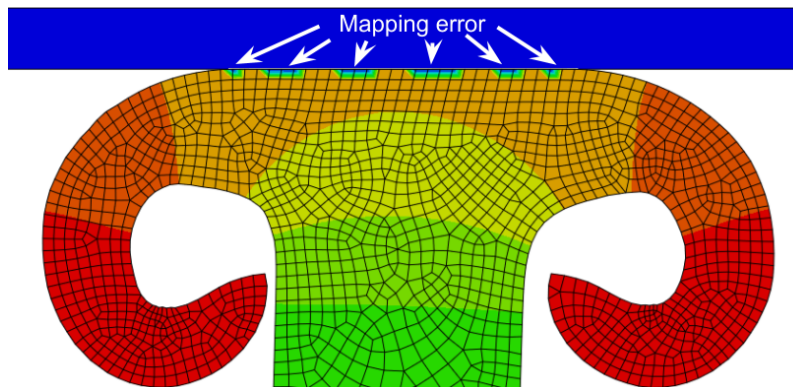


**Figure 4.8:** Example of mapping error on the temperature field in the rigid plane model.

## 4.5 Heat flux models and heat calibration

In this section the heat flux models will be evaluated. The simulations will be run with thermal simulations and will use a new geometry that more closely resembles the test pieces, see Figure 4.9. This geometry was delivered late into the project and has therefore not yet been tested with the remeshing methodology.

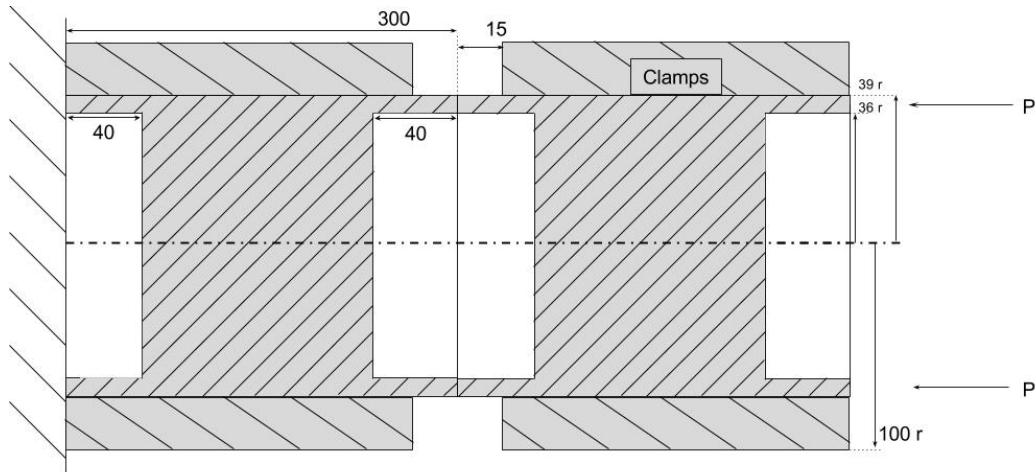


**Figure 4.9:** New geometry that is to be used in the heat calibration experiments.

As the heat flux model is for the most part unknown the shape of the fluctuations are to resemble that of Maalekian work in figure 4.10. The process parameters, pressure and velocity, will be assumed to vary as in figure 4.11.

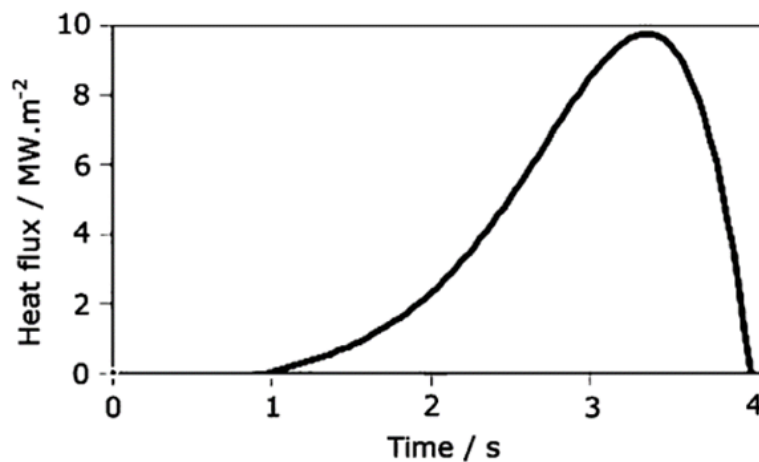


**Figure 4.10:** Maalekians proposed heat flux characteristics [6]

#### 4. 2D Axisymmetric Model for Calibration and Evaluation

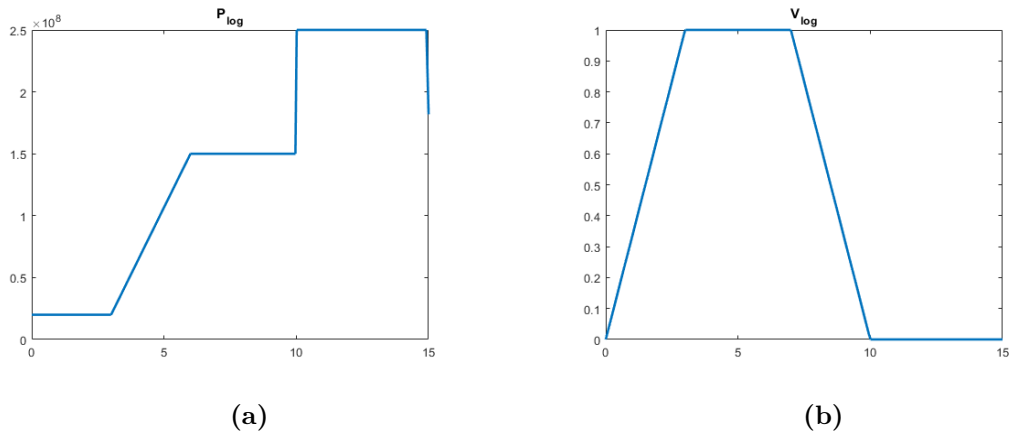


**Figure 4.11:** Assumed process parameters resembling that of the WRIST calibration test plan [25]. (a): Loading cycle. (b): Relative velocity cycle

Using the Tri-Linear model for this system results in figure 4.12 and 4.13. In these figures the effect of changing model parameters are shown, which is important to know when using the model to match test data. Changing the friction coefficient mainly effects how rapidly the temperature increases, while the change of  $T(\mu = 0)$  effects the maximum temperature the system will reach. This behaviour is highly unphysical as one would not expect  $\mu(T \rightarrow 1200) \rightarrow 0$  but rather that it gradually change into a visco-plastic friction model. The model will probably work well when calibrating the heat flux for a specific case, but as no physical behaviour is included the calibrated  $\mu$  will be completely fictive. It is shown in [7] that the friction coefficient is highly dependent on the load and the rotation speed. Therefore, despite being able to accurately represent one specific calibration case it might not transition onto other systems well, such as the geometry change to the rail or changes in process parameters.

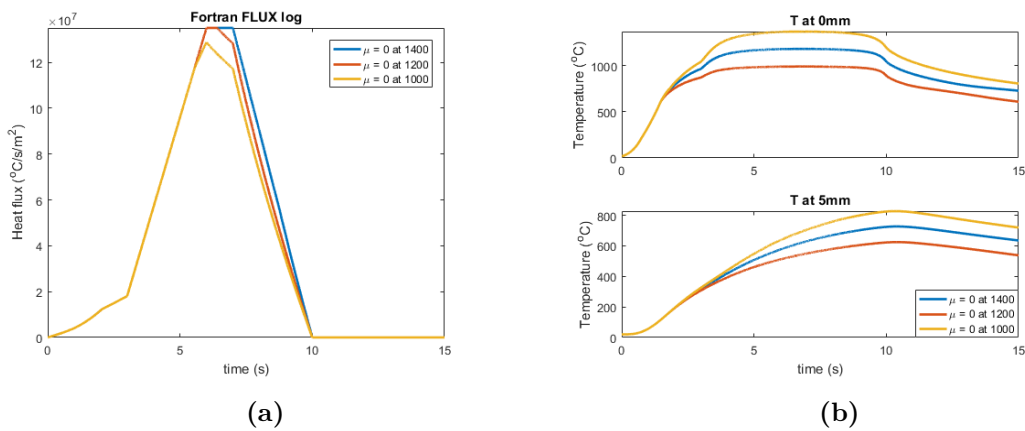


**Figure 4.12:** Behaviour of the Tri-linear model for different values of the  $T(\mu=0)$ . (a): Heat flux. (b): Temperatures. upper image: at contact surface. lower image: 5mm from contact surface.

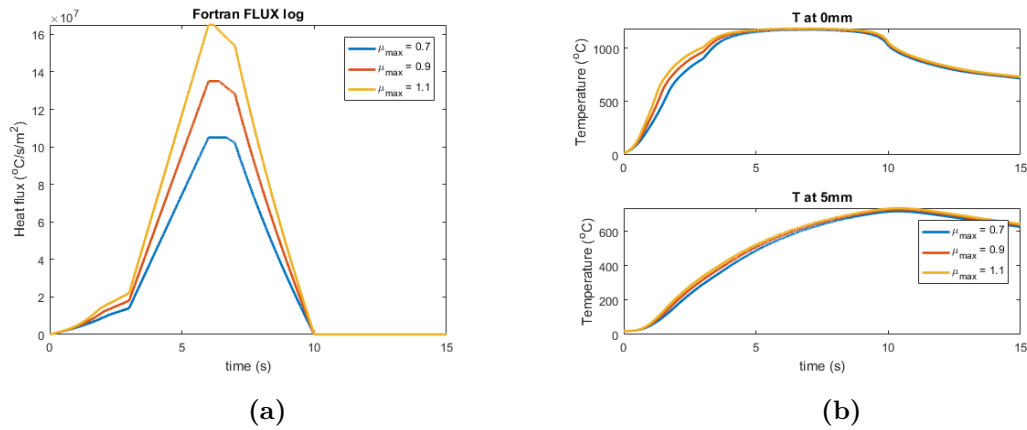


**Figure 4.13:** Behaviour of the Tri-linear model for different values of the maximum friction coefficients. (a): Heat flux. (b): Temperatures. upper image: at contact surface. lower image: 5mm from contact surface.

Using the Tau-model results in figure 4.14 and 4.15. The figures show that the Tau model is strongly dependent on what material model is used. None of the heat flux curves resemble that of Maalekians work at all and might therefore be considered to be inferior to the Tri-linear model at this point. There are several problems with using this model. It is difficult to determine when to consider the material to be considered to as fully plastic and also if the change will be be instant or gradual. It might be necessary to implement effects such as hardening or visco-plastic behaviour in order to get a reasonable result.

It would be reasonable to assume the Tau-models plastic flow rule becomes invalid as soon as the visco-plastic behaviour becomes important. Assuming that visco-plasticity becomes dominant at 70% of the melting temperature, that is about 1000°C, which is reasonable to assume as mention in section 3.1. This would mean that for the current loading scheme the Tau models flow rule becomes invalid almost as soon as it is applied, see figure 4.16 and 4.15. Which would explain the questionable behaviour of the heat flux, figure 4.15a.

Additional problems with this model is that it is hard to use as a calibration model. As the complexity that comes with the dependence of the yield stress will make it difficult to determine what parameter needed to be adjusted to archive realistic heat flux.

## 4. 2D Axisymmetric Model for Calibration and Evaluation

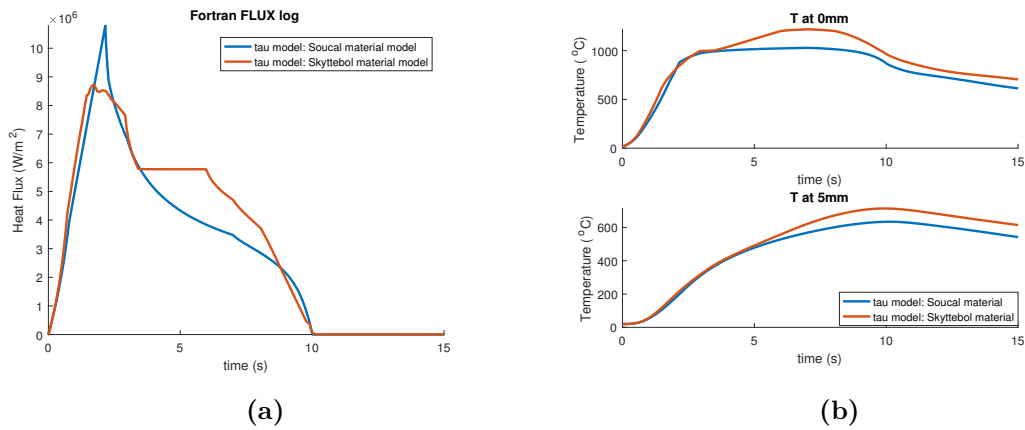


**Figure 4.14:** Behaviour of the Tau model for different material models. (a): Heat flux. (b): Temperatures. upper image: at contact surface. lower image: 5 mm from contact surface.

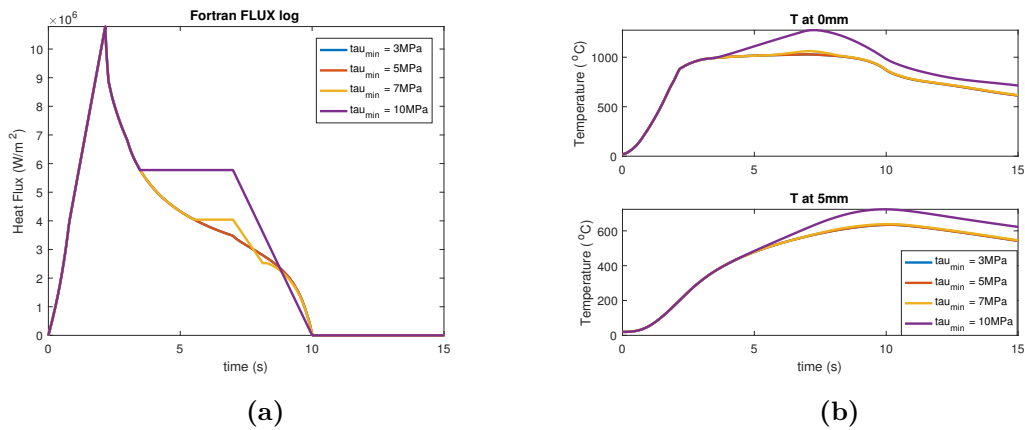


**Figure 4.15:** Behaviour of the Tau model for different values of the Min  $\tau_{y}$ . (a): Heat flux. (b): Temperatures. upper image: at contact surface. lower image: 5 mm from contact surface.

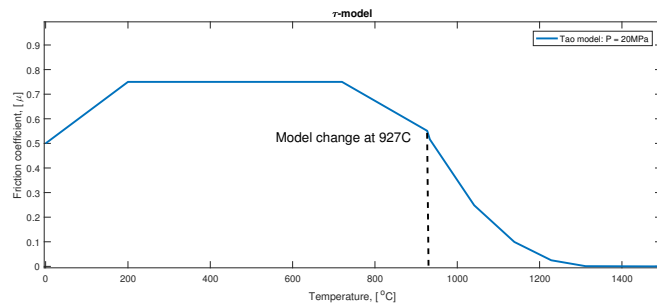


**Figure 4.16:** The image shows the model change in the Tau model for the given process parameters

## 4.6 Material model comparison

This section contains a comparison of the Skyttebol model with kinematic hardening and the Soucal visco-plastic, isotropic hardening model. The process parameters are such that it yield flash formations of reasonable size. In figure 4.18 the Soucal model which is the same as previously shown results, and in figure 4.19 is the Skyttebol model. In figure 4.17 an example of the behaviour of the flash formations during friction welding is shown.

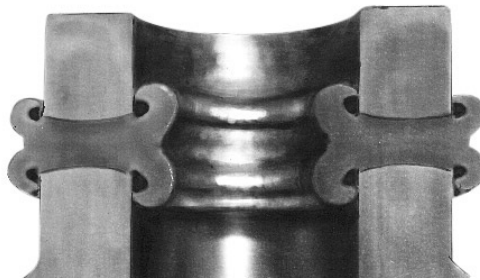


**Figure 4.17:** An example of flash formations during the friction welding process, cf. [26]

Despite that the process parameters differ largely between the simulations, the flash formations behaviour can be observed. In the simulations using the kinematic hardening Skyttebol model the flash formations does not curve as in the example in figure 4.17.

There are several possible causes for this. It could be due to that the Skyttebol model does not include visco-plastic behaviour which should be included for the working temperature of 1200 °C .

The behaviour of the yield model also has an effect on the lack of curvature in the Skyttebol flash formations. The bright orange material in Skyttebol has the same yield limit of 10 MPa as the red material in Figure 4.19. This lack of yield gradient probably has a large impact on the shape of the flash formations. In contrast the yield is reduced by  $\frac{1}{3.5}$  from bright orange to red in the Soucal model shown in Figure 4.18. Another thing to note is that the red material in Figure 4.19 is about 7.5 times stiffer then that of Figure 4.18.

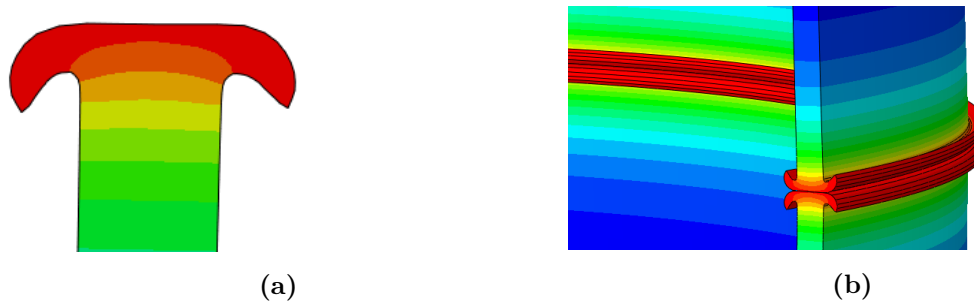


**Figure 4.18:** Rigid-Plane model: loading cycle 1,  $P_{Forge} = 150MPa$ , Soucal viscoplastic, isotropic hardening model. (a): Flash formations (b): 3D view of the flash formations

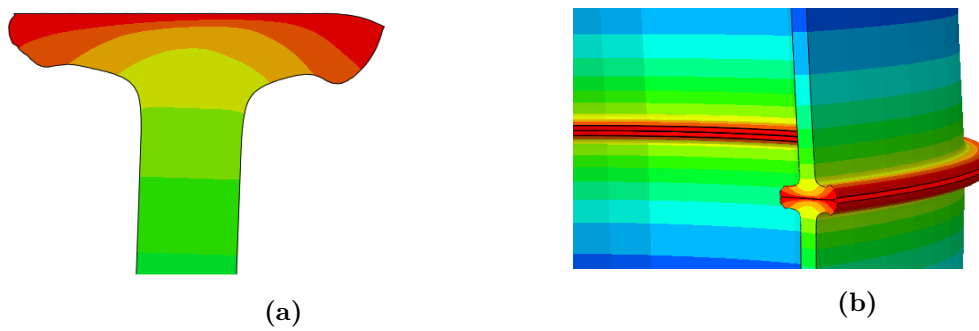


**Figure 4.19:** Rigid-Plane model: Skyttebol kinematic hardening model.  $P_{heating} = 2MPa$ ,  $P_{Forge} = 150MPa$  (a): Flash formations long load ramping times (b): 3D view of the flash formations Long load ramping times.

# 5

## Orbital Friction Welding of Rails

In this chapter simulations of orbital friction welding are described. A detailed model solely used for thermal analysis is described in section 5.1.1. The thermal simulations are used to study effects of varying process parameters and implemented thermal sinks. A simplified model is presented that has been used for uncoupled thermo-mechanical simulation of OFW. The mechanical simulations did not converge but serves to provide insight concerning modeling aspects.

### 5.1 Model Geometries

This section aims to describe the model geometries used. The two models presented are referred to as the *full model* and the *simplified model*.

#### 5.1.1 Full model

The model for orbital friction welding is set up in accordance with specifications from the wrist project [11]. The UIC60 rail profile is extruded creating the rail and the model consists of five different geometries and seven different parts, see figure 5.1a. Two symmetry conditions are used reducing the model to 1/4 of its original size, see figure 5.1b.

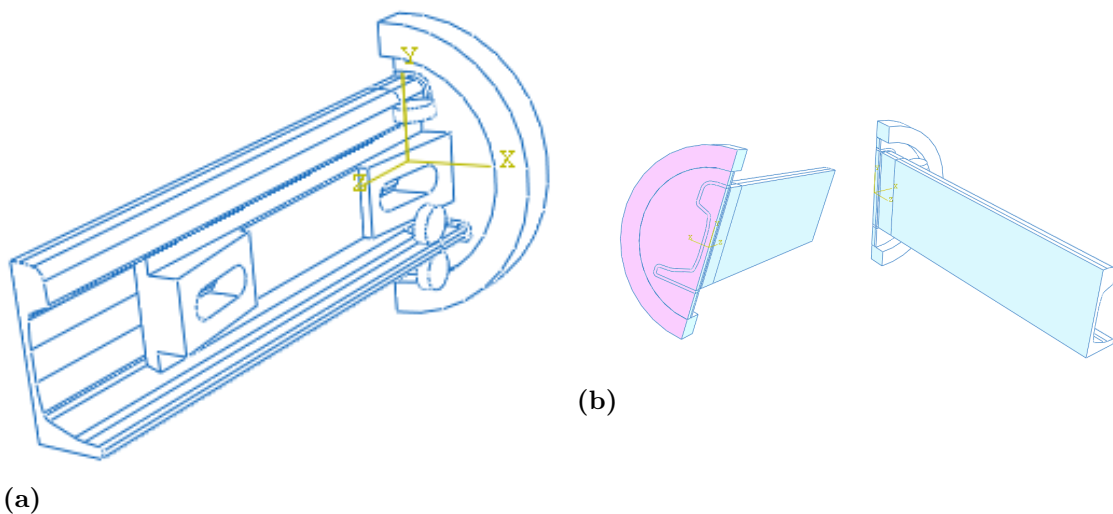


**Figure 5.1:** (a) *full model*. (b) *full model* symmetry surfaces.

### 5.1.1.1 Thermal sinks: full Model

It is of interest to study the effects on the temperature field of clamps fixating the disc and rail, specified by the WRIST project [11]. The clamps are modeled as sinks of thermal energy which influence the temperature field. Two major sinks are added one for the rail referred to as *rail clamp*, see figure 5.2a and one for the disc referred to as *disc clamp*, see figure 5.2c. The rail clamp has a thickness of 20 mm and width of 100 mm at its lower line seen in figure 5.2d and is extruded 460 mm.

The disc sink is a thick short tube cut in half at the x-symmetry line with an inner radius of 125 mm (fitting the disc) and an outer radius of 160 mm that is extruded 40 mm, see figure 5.2c

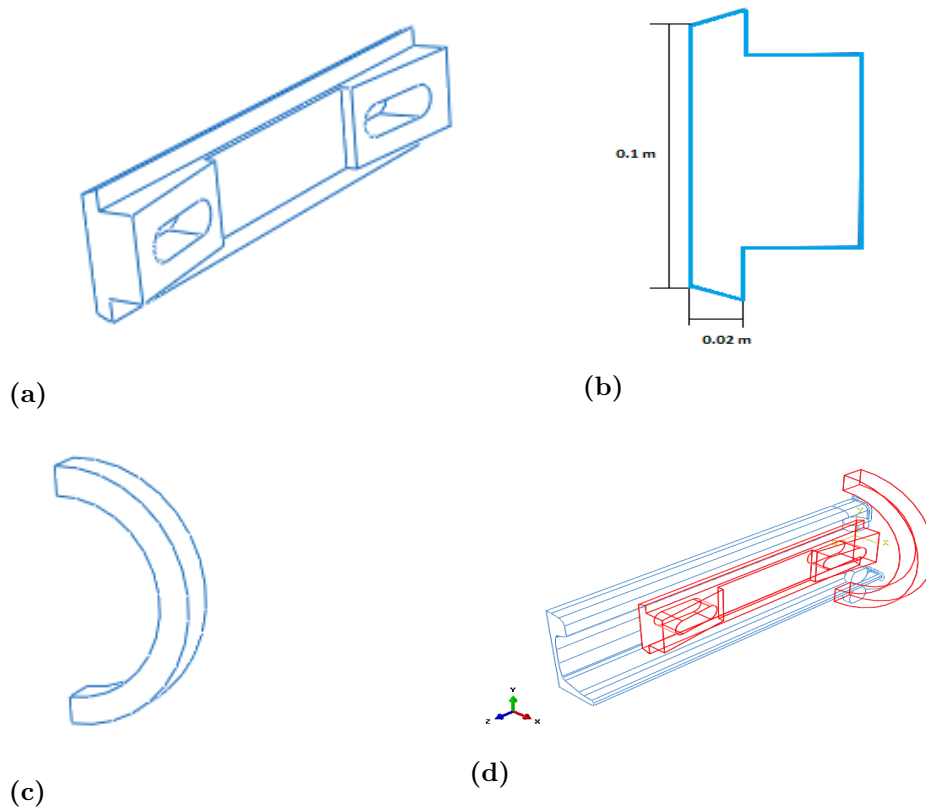


**Figure 5.2:** Clamps. (a) Rail clamp. (b) Specified thickness and width of the rail clamp. (c) Geometry of disc sink. (d) Positions of major clamps

Three smaller cylinders are also added to the model simulating the effect of smaller contacts holding the rail in place, these are referred to as cylinder sinks. They have a radius of 20 mm and are 14 mm thick. The cylinder sinks are positioned at the second partition line of the rail 50 mm from the rail contact surface.

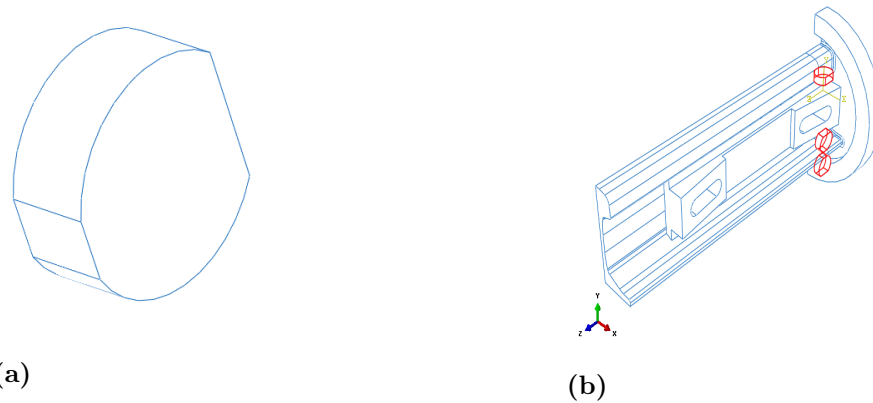


**Figure 5.3:** Cylinder sinks. (a) Geometry of cylinder sinks (b) Positions of cylinder sinks

#### 5.1.1.2 Rail and disc: full Model

The UIC60 rail profile is extruded to 0.6 m minimizing size of the model while assuring that influence of the boundary is minimal. For simulations with longer heating and cooling phases the rail profile might need to be extended further. The extruded rail profile is partitioned in three sections enabling control of the mesh size where large gradients are expected, see figure 5.4. The partitions are positioned 5 mm and 50 mm from the contact surface to the disc.

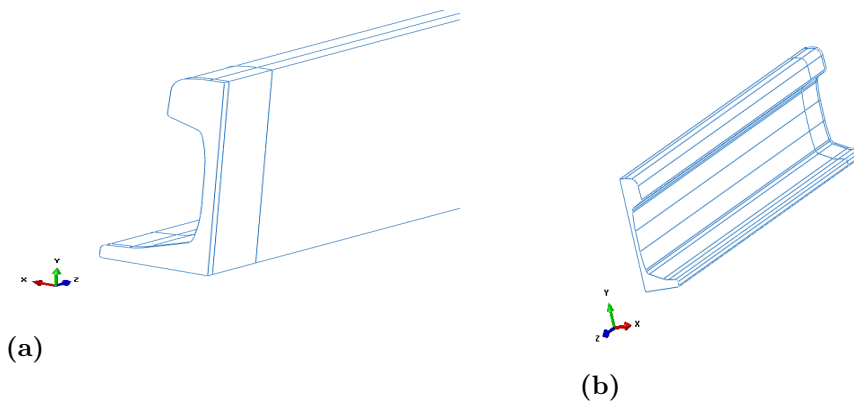


**Figure 5.4:** Rail geometry. (a) Rail, showing partitions. (b) Rail second view.

The disc has a radius of 125 mm and a thickness of 15 mm yet models the behavior of a disc with 30 mm of thickness due to the symmetry condition, see figure 5.5. It is partitioned to fit the rail contact surface, specify surface subjected to heating with an offset of 5 mm and the disc is sliced 5 mm from contact surface enabling mesh control.

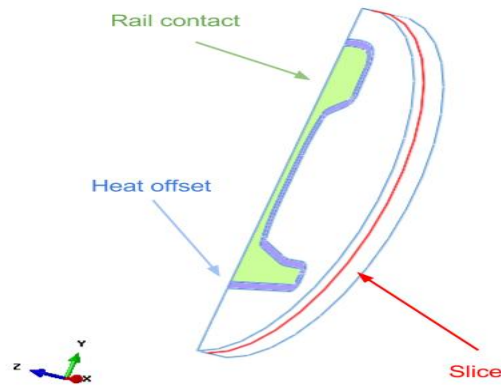


**Figure 5.5:** Disc specification. Figure showing the sections of the disc.

### 5.1.2 Simplified geometry

The simplified model is used in the thermo-mechanical simulation. The geometry differs from that of the full model concerning length of the rail as well as thickness and radius of the disc. One goal of this project has been to carry out mechanical simulation for orbital friction welding of rails. However, due to numerical issues, mechanical simulations have only been possible using this simplified model.

The simplified model consists of two parts, the cut rail and the disc, assembled in the manner depicted in Figure 5.6. The UIC60 rail profile is extruded 0.3 m and partitioned in 3 pieces, 5 and 15 mm from the contact surface, enabling control of mesh size in regions which will be subjected to high temperatures and subsequently large gradients. The disc, for the simplified model, has a radius 0.2 m and a thickness of 20 mm modelling the behaviour of a disc with 40 mm of thickness due to the symmetry condition. It is partitioned similarly to the disc of the full model yet is partitioned (sliced) one additional time through its thickness giving the model 3 layers. The partitions (slices) are made at 5 and 10 mm from the contact surface.

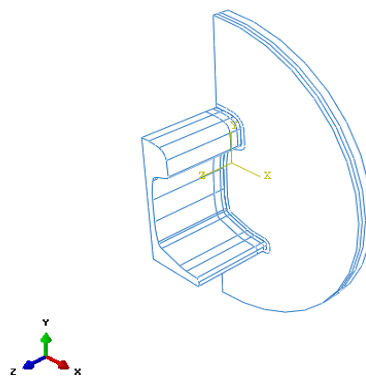
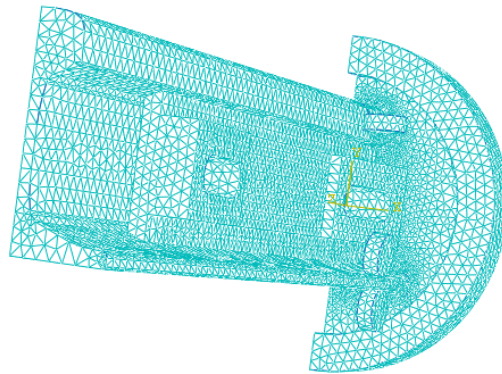


**Figure 5.6:** Simplified Rail model

## 5.2 Meshes

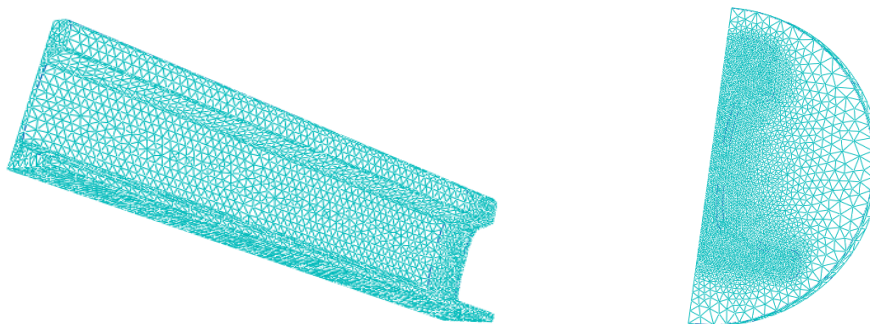
Regarding the full model, size of elements varies in the meshes with side lengths of elements ranging from approximately 1.5 mm in finer regions to 15 mm in coarser regions. Due to the rail profile shape, usage of larger elements will produce a poor mesh. See figures 5.7 and 5.8. A brief mesh convergence study was performed, see appendix E, confirming conclusions by Bisschop and Oddy cf. [3]. The report, concerning very similar thermal simulations, concluded that mesh convergence was reached for meshes with an element side length finer than 8 mm.

Tetrahedral 4-node linear elements are used for all thermal analysis by the name of DC3D4 in Abaqus, see Abaqus manual [19], which where shown to be adequate in [3].



\*

**Figure 5.7:** Full mesh shown in figure.



(a)

(b)

**Figure 5.8:** (a) Rail mesh. (b) Disc mesh.

10 node quadratic tetrahedron elements are used for the mechanical analysis, denoted in Abaqus as C3D10. Quadratic elements has been observed to behave in the sought characteristic behavior, see section 4.6, regarding flash formations in [4]. The

mesh for the simplified model is shown in figure 5.9 with side lengths of elements ranging from approximately 2 mm in finer regions to 15 mm in coarser regions.

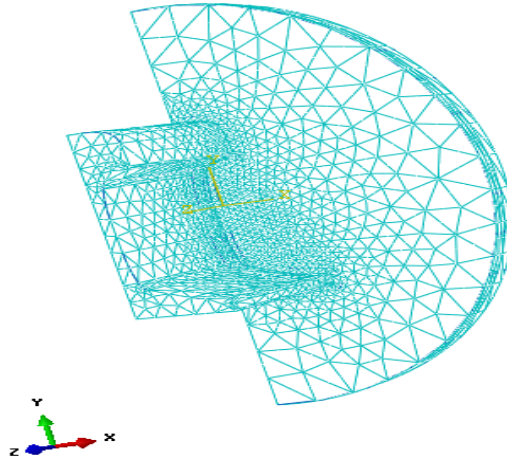


**Figure 5.9:** Mesh of the simplified rail model

### 5.3 Thermal modeling

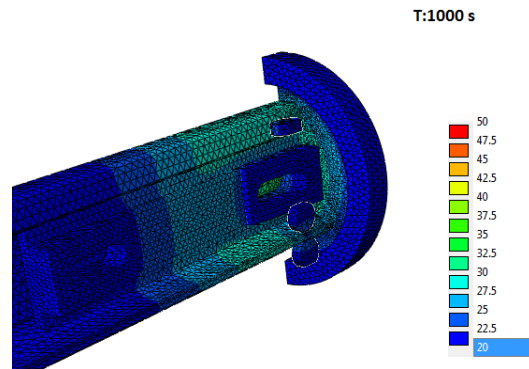


**Figure 5.10:** Temperature field visualized at the end of heating phase

Thermal modeling serves to determine material properties obtained from the process and is critical for the mechanical simulation. Some conclusions regarding varying effects can be made since material parameters such as thermal conductivity and specific heat are well defined, yet there are uncertainties regarding the heat flux. The purpose of these simulations is not to evaluate modeling aspects. Instead effects of process parameters and thermal sinks are evaluated.

All simulations are solved implicitly using full-newton solution technique. The initial increment size is set to 0.02 seconds with the maximum allowed temperature difference per increment set to 20 °C. If a higher allowed temperature difference per increment is set in combination with larger time steps the simulations would

become numerically unstable.

Material parameters used are found in appendix F. Density is set to that of steel  $7850 \text{ kg/m}^3$ . The thermal simulations are divided in to 3 steps namely the heating phase, the forging phase and the cooling phase, as described in section 5.3.1. Heatflux is only applied during the heating phase while the subsequent steps are cooling phases where the heat spreads throughout the material and into boundary conditions. The heat flux generated from frictional forces, has the disc spins, is modeled by imposing a heatflux condition on the connecting surfaces between the rail and disc. The heatflux condition or thermal load is applied on surfaces as shown in figure 5.11a. Heating surface on the disc is modified with an offset of 5 mm to the contact surface which is the true surface affected by a heatflux since the disc is in motion, see figure 5.11b. All rail simulations use the trilinear model for the heatflux, as described in detail in Section 4.5.

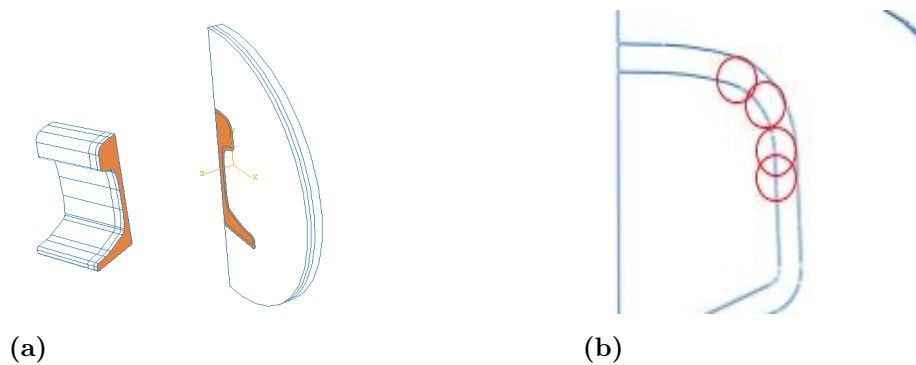


**Figure 5.11:** Heat surfaces. (a) Surfaces with applied heat flux. (b) Orbital motion increasing heating surface on disc

A contact condition is imposed on contact surfaces with a conductivity of  $100000 \text{ K}(mW)^{-1}$  assuming perfect conductivity, see figures 5.12. Each contact has high pressure applied removing imperfections, therefore connections are assumed to be in perfect contact. Since the thermal simulation is separate from the mechanical simulation the contact surfaces does not vary in time.

Boundary conditions of  $20 \text{ }^\circ\text{C}$  are set on outer surfaces of the thermal sinks, see figure 5.13. These sinks are connected to even larger geometries which are considered to have an infinite thermal capacity.

Heat convection to air is modeled using a surface film condition with a conductivity of  $6.8 \text{ K}(W)^{-1}$  and a sink temperature of  $20 \text{ }^\circ\text{C}$ . The disc symmetry surface is insulated as well as the rail cut surface. The initial temperature of the entire model is set to  $20 \text{ }^\circ\text{C}$ .

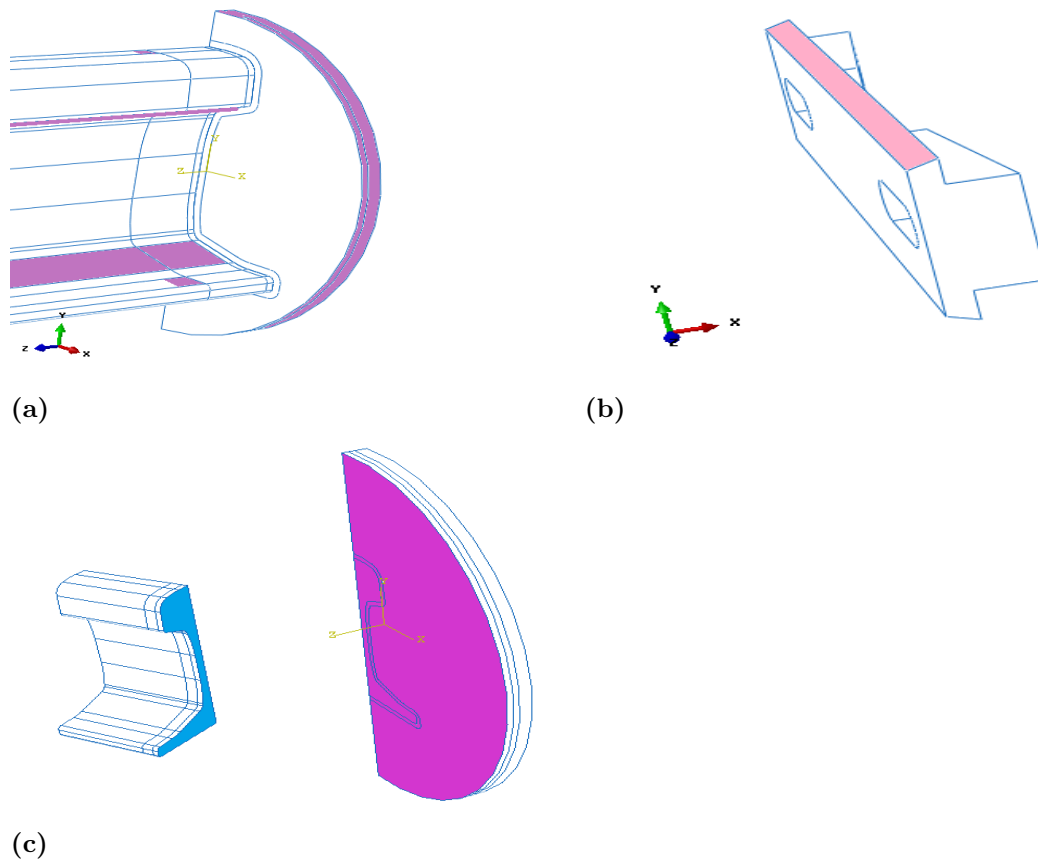


**Figure 5.12:** Contact surfaces. (a) Contact areas on the rail and disc to thermal sinks. (b) Contact area on the rail clamp. (c) Contact surfaces concerning rail to disc.

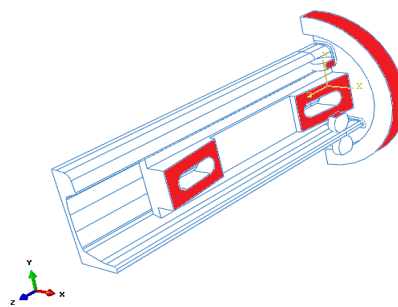


**Figure 5.13:** Temperature boundary conditions on thermal sinks

### 5.3.1 Simulation schemes

The simplified model is not of particular interest regarding evaluation of the thermal results, but the results from the thermal simulation are used in the mechanical simulation. The settings for thermal simulation of the simplified geometry is therefore also specified.

The trilinear heatflux model, see Section 3.5, is implemented using 3 different time schemes in 6 different simulations, the time schemes for the heatflux are 5, 9 and 20 seconds long. See figures 5.14a through 5.14d.

1. Heating phase: 5, 9 or 20 seconds
2. Forging phase: 3.5 or 6 seconds
3. Cooling phase: 1200 seconds

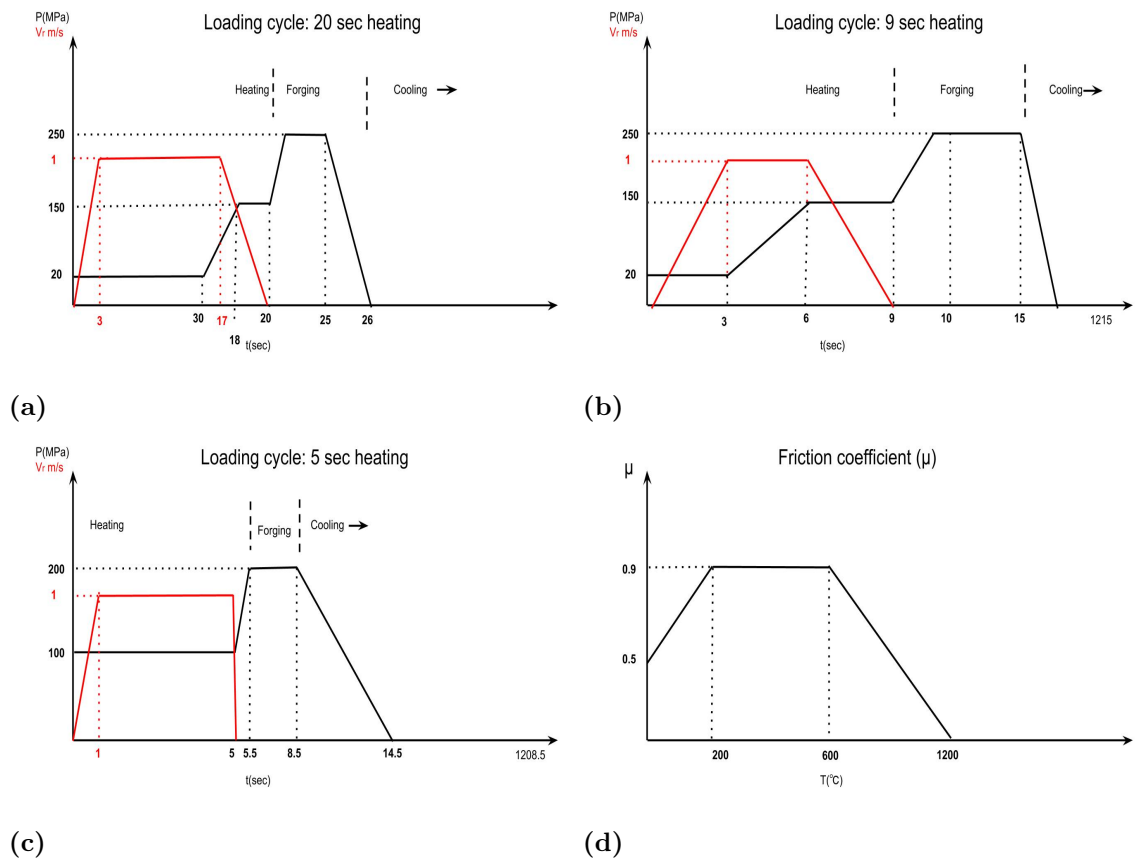


**Figure 5.14:** (a) Process parameters vs time, 20 sec heating phase (T4 and T5). (b) Process parameters vs time, 9 sec heating phase, (T1 to T3). (c) Process parameters vs time, 5 sec heating phase, (M1). (d)  $\mu$  vs  $T(^{\circ}\text{C})$ , trilinear model

The 6 different simulation schemes all with 1200 seconds long cooling phase are as follows:

- M1. Simplified Rail geometry, 5 seconds heating phase, 3.5 seconds forging phase.
- T1. Full model, with thermal sinks, 9 seconds heating phase, 6 seconds long forging phase.
- T2. Full model, only with disc sink, 9 seconds heating phase, 6 seconds long forging phase.
- T3. Full model, without thermal sinks, 9 seconds heating phase, 6 seconds long forging phase.
- T4. Full model, without thermal sinks, 20 seconds heating phase, 6 seconds long forging phase.
- T5. Full model, with thermal sinks, 20 seconds heating phase, 6 seconds long forging phase.

### 5.4 Mechanical modelling

The model represents OFW of rails. The temperature field is imported from the thermal analysis of the simplified model using process parameters in accordance with the M1 simulation scheme. The material parameters are highly dependent on temperatures ranging from 20 to 1200 °C, the stiffness of the model is therefore time dependent. The EC3 yield model is used, see appendix F or section 3.3.1.

The equilibrium equations are solved using a full Newton solution scheme.

A pressure load is imposed on the rail cut depicted in figure 5.15a with varying amplitude, see figure 5.15b. The mechanical simulation follows the M1 simulation scheme. Step 1, heating phase, during which a load is ramped up to 30MPa. Step 2, forging phase, where most of the deformations occur due to a high load of 200MPa lasts for 3.5 seconds. Lastly step 3, cooling phase, during which the model is unloaded during 6 seconds and cooled to recognize residual stresses inherited from the process. Nodes are locked in x and y on the loading surface, which are the tangential directions of the surface, to ensure that the rail does not drift in those directions. All nodes are locked in normal directions on disc and rail symmetry surfaces shown in figure 6.14a.

For contact modelling a master and slave condition is implemented between the rail contact surface and the disc surface depicted in figure 5.16b. The tangential behavior is set to *Frictionless* during heating and forging phases while set to *Rough* during the cooling phase. The normal behavior is set to *Hard contact* allowing separation during heating and forging phases while not allowing separation during the cooling phase. For more information regarding the mechanical contact conditions see ABAQUS user manual [8].

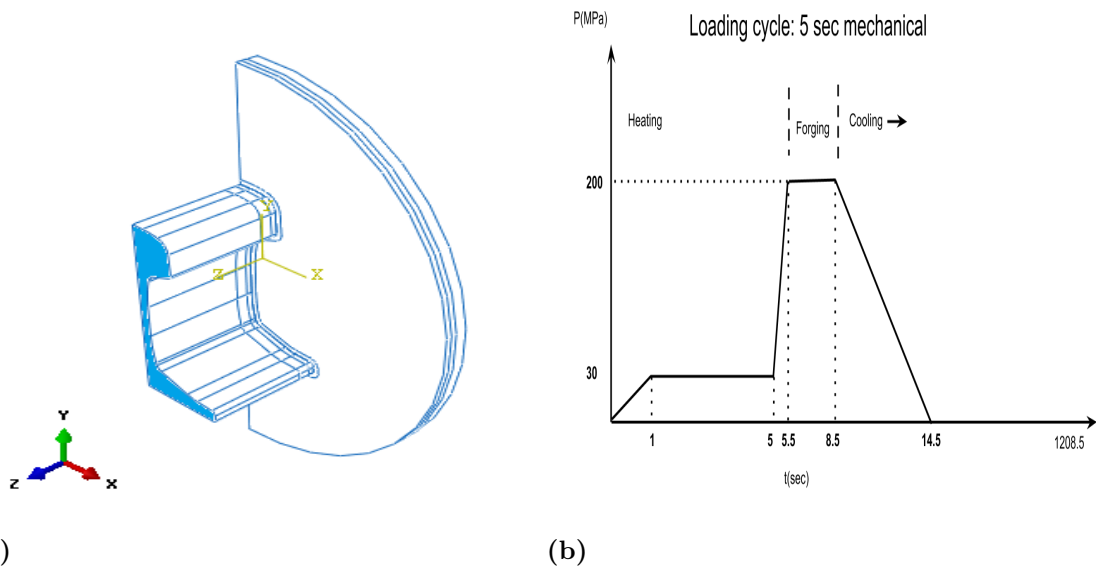


**Figure 5.15:** Figures showing loading surface and loading cycle. (a) Rail loading surface. (b) Loading cycle.

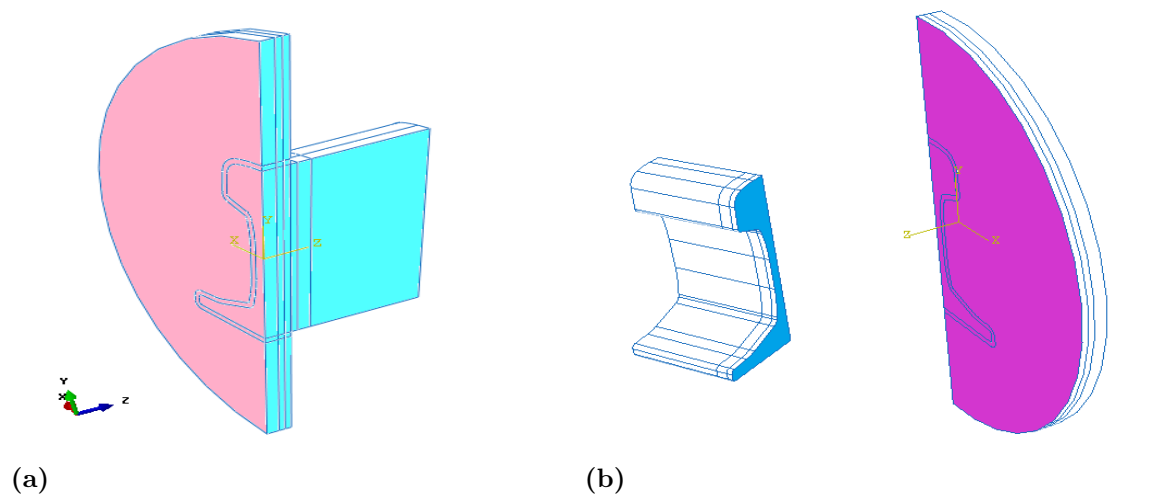


**Figure 5.16:** Figures showing symmetry and contact surfaces. (a) Symmetry surfaces of simplified model. (b) Contact surfaces of simplified model.



# 6

## Thermal and mechanical results from modeling of orbital friction welding

In this chapter results from modelling of Orbital friction welding are presented, evaluated and discussed. The chapter is divided in two sections. Section 6.1 addresses thermal results and section 6.2 mechanical results.

### 6.1 Thermal results

Results from 5 different simulations are presented regarding the Full model to evaluate influences of thermal sinks and length of the heating phase. Simulations presented have used schemes T1 to T5, see section 5.3.1. The simplified rail geometry is not evaluated with respect to the thermal analysis in this report, thermal results from the simplified model are however used in the mechanical model.

The temperature field with respect to time is of importance when evaluating the weld. As stated the HAZ is desired to be as small as possible and the cooling rate affects the material characteristics, see section 3.2.1. Using a CCT diagram material properties can be evaluated from the obtained cooling rate at each point in the HAZ. The influence of process parameters and geometrical aspects, such as thermal sinks, on the temperature field are studied. This section begins with a description of how results are presented (defining nodes), thereafter important results are presented and lastly modeling errors and discrepancies are discussed.

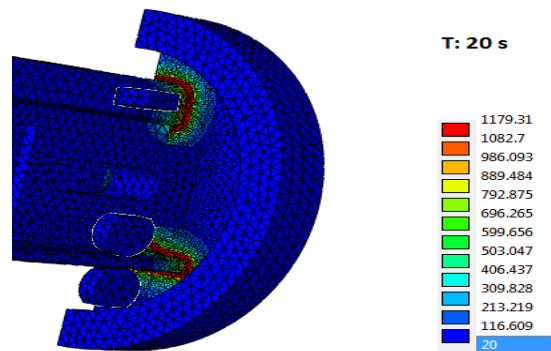


**Figure 6.1:** Temperature field visualized at the end of heating phase

### 6.1.1 Specification of nodes used in evaluation

Results with respect to the full model are taken from nodes at 6 lines. In this report nodes are defined by which line they belong to and their distance to the starting point. In figures 6.2 the bottom line is shown (denoted bL). Four more lines are used to define nodes namely the clamp line (denoted cL) and the disc lines (denoted dL1, dL2, dL3) shown in figure 6.4.

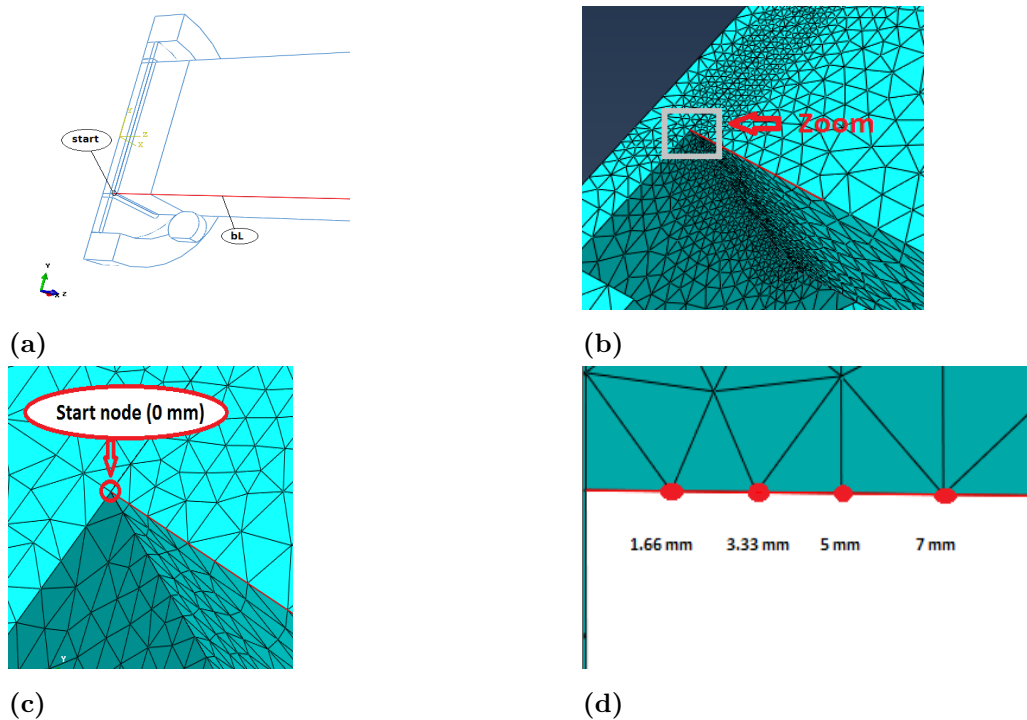


**Figure 6.2:** Figures describing system for defining nodes. (a) bL line on Rail. (b) bL line shown in mesh. (c) Closer look at bL line with starting point circulated. (d) Figure of how nodes are defined by their distance to the starting point.

To evaluate the impact of the clamp imposed on rail the results from nodes on the clamp line (denoted cL) and normal line (denoted nL) are used, see figure 6.3. Distances on cL are given as distance to the disc (the heat source), see figures 6.3a, while line nL is parallel to and 5 mm from the disc. The start point on nL are right at the edge of the clamp shown in figure 6.3b.

Temperature on the disc are evaluated at lines located on the x-symmetry plane of the disc depicted in figure 6.4. They are referred to as dL1, dL2 and dL3, dL being short for disc lines. Starting points for dL2 and dL3 are just at the contact-surface towards the rail while the starting point dL1 is 5mm away from the contact surface. Evaluated nodes are defined by their distance to the starting point along its respective line. No nodes on dL1 reach transformation temperatures during any simulation, therefore no results are presented from that line.

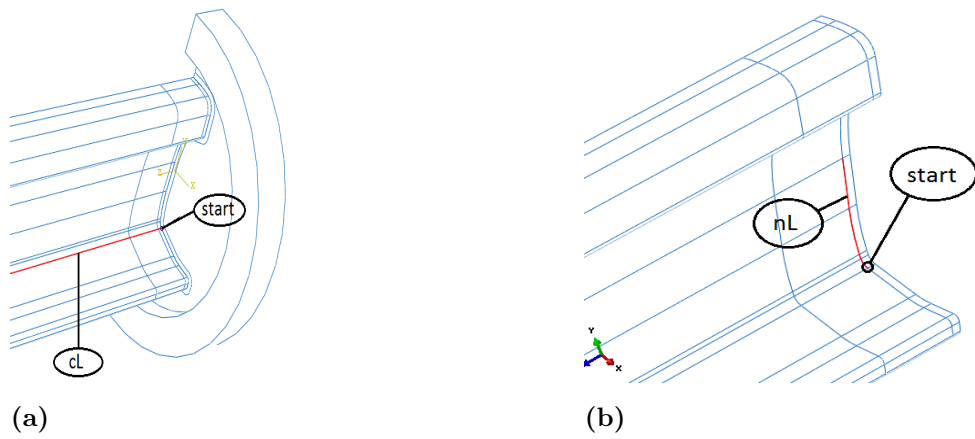


**Figure 6.3:** Specified lines used for evaluation shown as red lines. (a) cL line. (b) nL line

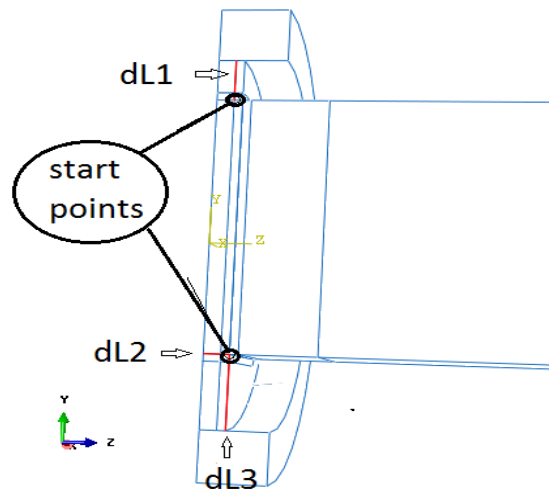


**Figure 6.4:** dL lines shown in red with starting points circled

### 6.1.2 General results, HAZ, cooling rates

The HAZ, defined as parts which have reached 800 °C or higher, are shown in figures 6.5 for a 9 second long heating phase, T1-T3.

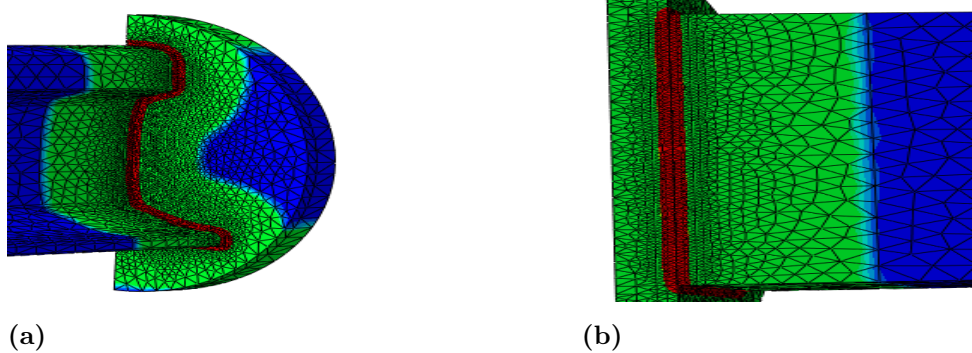


**Figure 6.5:** HAZ visualized in red for T1 simulation. (a) HAZ on rail and disc, (b) HAZ on x-symmetry surface.

The HAZ is approximately 3.3 mm for T1-T3 simulations and 5 mm for T4 and T5 simulations, see figures 6.6 and 6.7. The temperature variations are evaluated along bL for the rail and along dL2 for the disc. Results along dL2 are seemingly identical to those on bL at the same distance to the heat source. For simulations presented in this thesis, the HAZ extends an equal length into the disc as through the rail, which is not the case for any given process parameters.

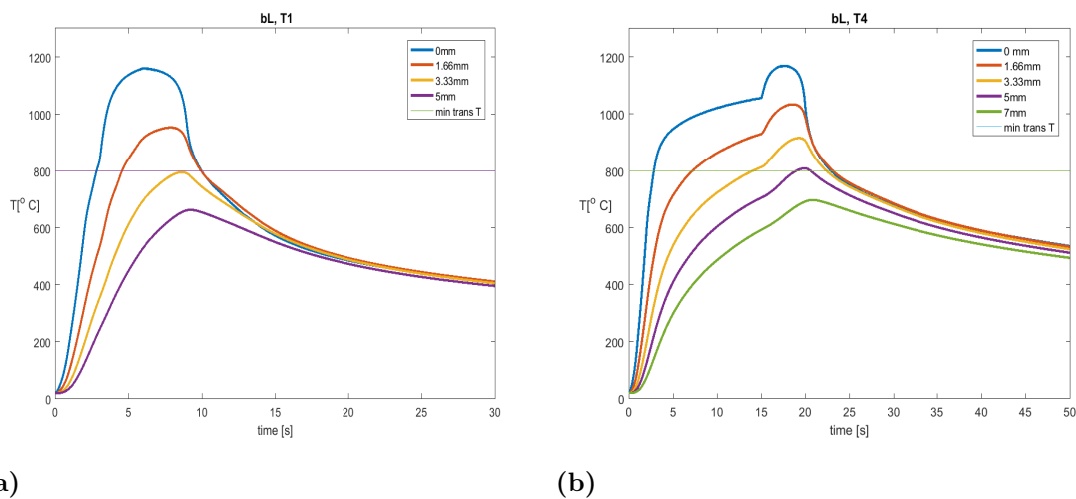


**Figure 6.6:** Graphs showing variations in temperature along bL for simulations T1 and T4 for comparison on the size of the HAZ. (a) Temperature variation along bL for T1, (b) Temperature variation along bL for T4.

## 6. Thermal and mechanical results from modeling of orbital friction welding

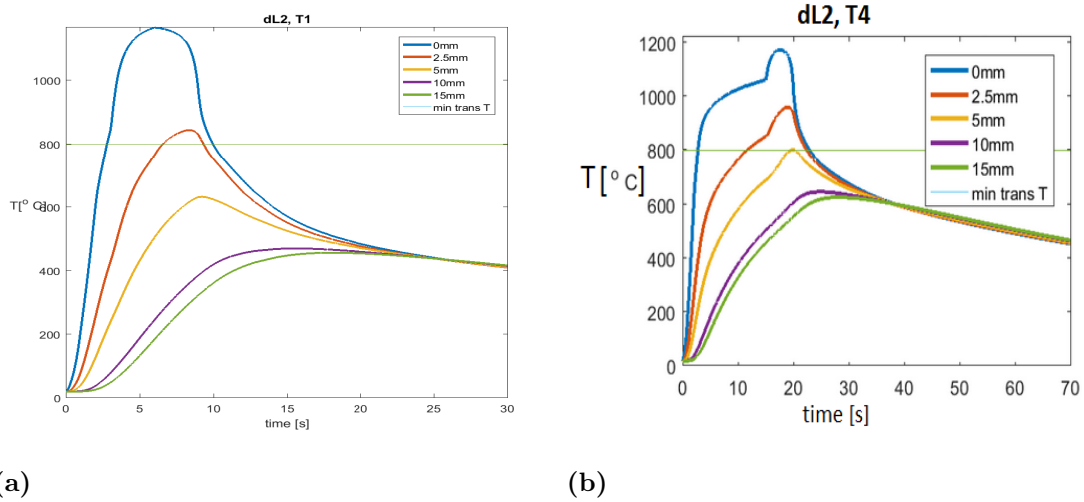


**Figure 6.7:** Graphs showing variations in temperature along dL2 for simulations T1 and T4 for comparison on the size of the HAZ. (a) Temperature variation along dL2 for simulation T1 (b) Temperature variation along dL2 for simulation T4.

A vast difference between process parameters used is the cooling rate. The cooling rate decreases with an increasing heating phase, see figure 6.8b. More than 70 % martensite is expected with process parameters set according to T1, T2 and T3. Although large portions of martensite are not desirable the HAZ is smaller relative a longer heating process. For the 20 seconds long heating phase (T4 and T5) mostly pearlite (80 %) is expected with a small portion of martensite (10 %) and bainite (10 %). This could be deemed as acceptable yet the HAZ is in return larger and the process time is increased. How the microstructure is determined from a CCT diagram is explained in section 3.2.1.

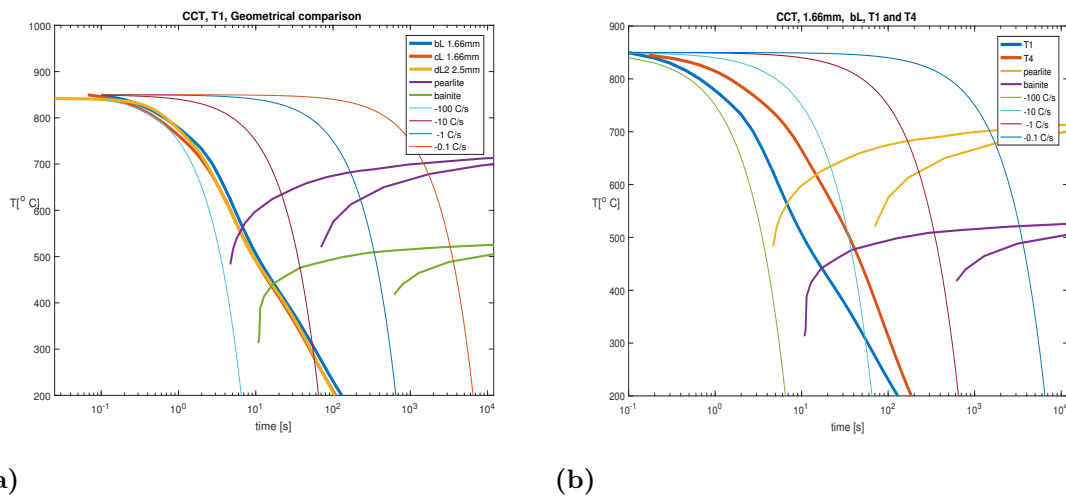


**Figure 6.8:** (a) CCT diagram comparing cooling rates at 3 different points concerning simulation T1. (b) CCT diagram comparing cooling rates between simulations T1 and T4

The cooling rate is seemingly identical concerning nodes inside the HAZ for each simulation separately, see figure 6.8a. There are some minor discrepancies regarding this statement, see section 6.1.4. The micro-structure composition is homogeneous within the HAZ and can therefore be evaluated using only one node. The thermal sinks does however have an effect on the HAZ and the cooling rate which cannot be evaluated using solely one node.

### 6.1.3 Effects of rail clamps

Effect of the rail clamps with respect to HAZ and cooling rate are evaluated along line nL and cL shown in figure 6.9b. The rail clamp influence the temperature field and acts as a thermal sink absorbing energy, decreasing temperature and increasing the cooling rate. Again differences in cooling rates insignificant with respect to position inside the HAZ demonstrated in figure 6.9a. In figures 6.10a and 6.10b results from T1 and T4 are presented for nodes along cL. Both simulations have sinks implemented and differ with respect to length of the heating phase. The HAZ is approximately 2 mm in depth (along cL) for simulation T1 while it is 3.33 mm in depth for T4. The HAZ is approximately 30 % smaller for zones in close proximity to the rail clamp.

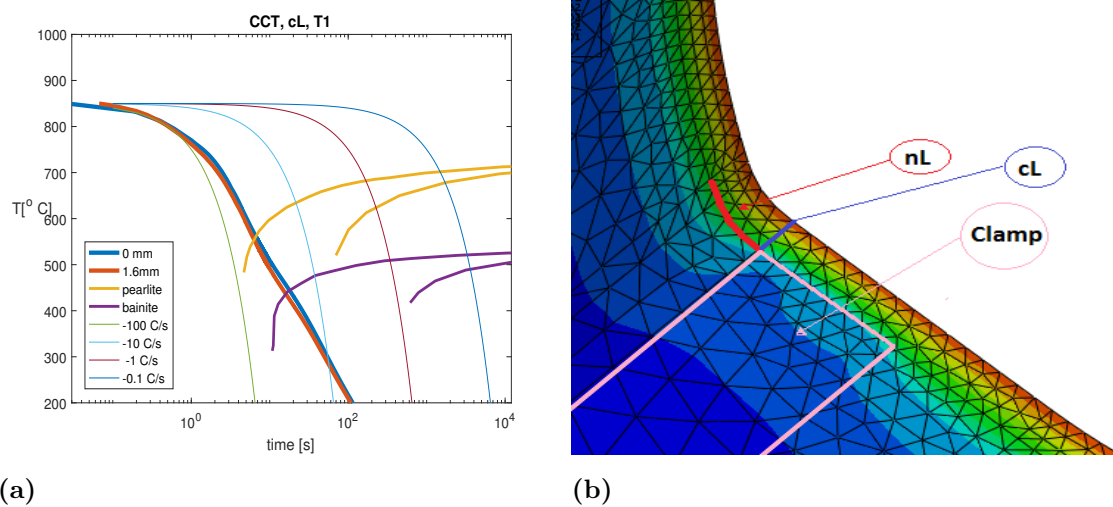


**Figure 6.9:** Evaluation of rail clamp effects. (a) CCT diagram comparing cooling rates at different nodes along cL for simulation T1. (b) Temperature field visualized at end of heating phase demonstrating positions of lines with respect to rail clamp.

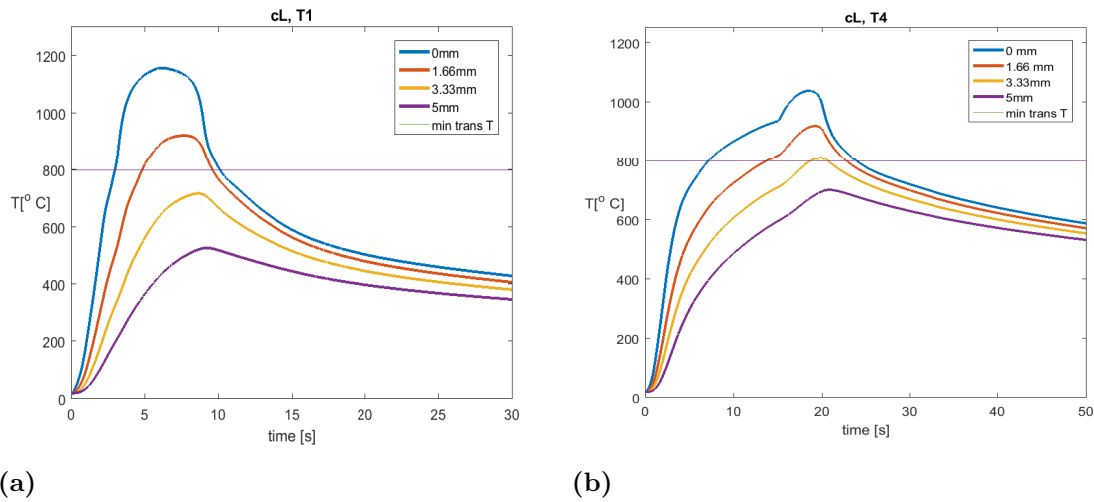


**Figure 6.10:** Evaluation of rail clamp effects. (a) Temperature variation along cL for simulation T1 (b) Temperature variation along cL for simulation T4.

Zones in close proximity to the rail clamp are effected as stated. To quantify the extent of this influence nodes on line nL are evaluated. Along line nL the differences in temperature decreases with increasing distance to the (rail clamp), see figure 6.11a. The maximum temperature difference along line nL is 155 °C and occurs at the end of the heating phase of simulation T4 for the node in direct connection to the rail clamp. At a distance of 9 mm to the rail clamp its influence is insignificant. The thermal sinks do effect the cooling rate but not in a substantial way on a logarithmic scale such as the CCT diagram. Effects on the HAZ and cooling rate of the rail clamp for distant zones are negligible and shown in appendix D.5.

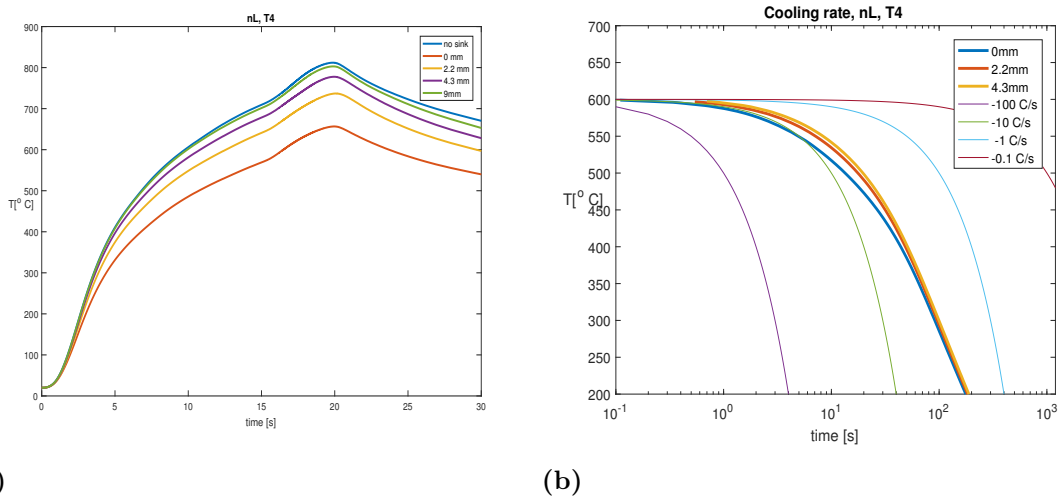


**Figure 6.11:** (a) Temperature variation along nL for simulation T4 (b) CCT diagram comparing cooling rates at different nodes along nL for simulation T4.

#### 6.1.4 Modeling errors and discrepancies

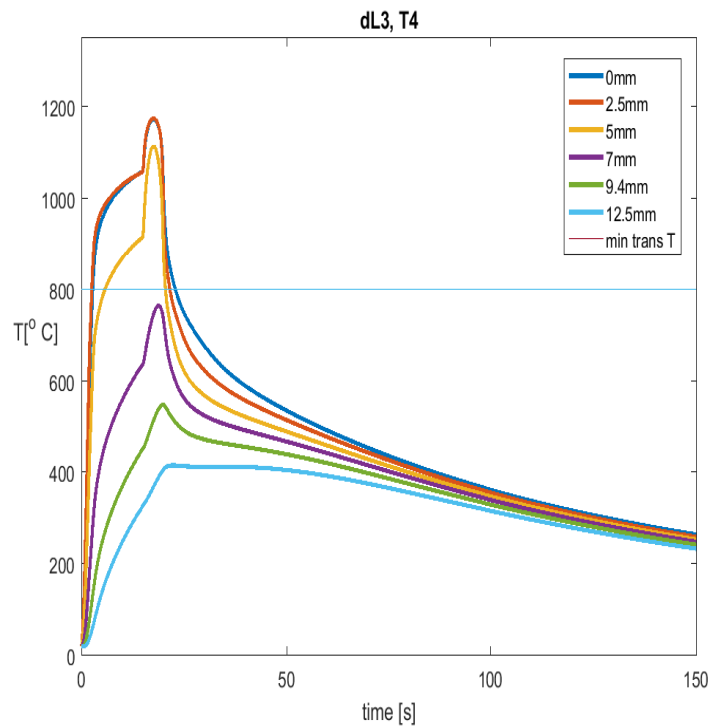
Overall thermal simulations presented are numerically stable and results correspond well to those found in studies such as [1]. There are however some observed discrepancies.

The heat flux dependence on process parameters such as velocity and pressure is highly uncertain for temperatures above 800 °C. The used heat flux model could be a source of error.

Thermal simulations presented does not include geometrical changes during the welding process. Simulations presented are not thermo-mechanical. Large deformations will effect the results which have not been evaluated.

The contact condition imposed between the rail and the disc is observed to effect the heat flux, which was studied in [3]. The temperature is slightly higher during the heating phase at the heat flux offset surface than on the contact surface. This can be observed in Figure 6.12, the node located 2.5 mm on dL3 is at the centre of the heating offset where the contact condition is not implemented and the node located at 0 mm is effected by the contact and heat flux condition.

It is concluded that the cooling rate does not vary within the HAZ. This is not true at the edge of the heat flux surface on the disc. Related zones will be cut away finalizing the weld producing a uniform profile of the railway and are therefor not of great interest. However, along dL3 temperature gradients are larger and the cooling rates are higher in comparison to results presented on dL2, cL, bL or nL. Differences in cooling rate are significant on line dL3 where the temperature gradient is very large around 5 mm from the rail, see Figure D.7. These results imply that the cooling rate inside the disc varies in the radial direction of the disc, especially close to the edge of the heating surface. These differences in cooling rates and temperature variation could be due to a modeling error. It is unrealistic that the heat flux is constant over the offset surface, which models effects of the orbital spin shown in Figure 6.13a. The heat flux should decrease linearly to zero at a outer line as in Figure 6.13b. The results regarding cooling rates on dL3 are therefore inconclusive.



1

**Figure 6.12:** Temperature variation along dL3 for simulation T4.

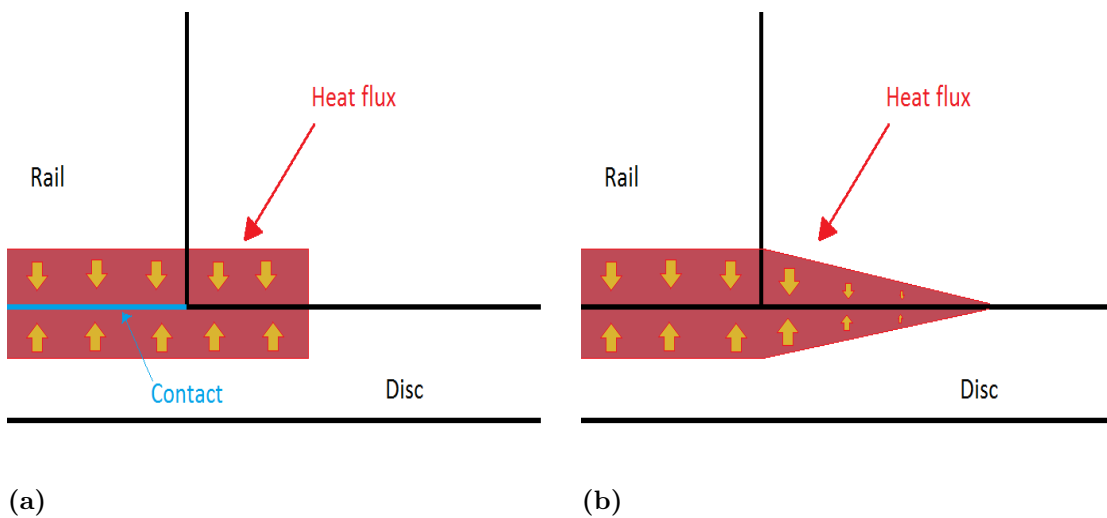


**Figure 6.13:** Figures demonstrating modeling errors of contact condition and offset heatflux surface (a) The uniform heatflux over the offset implemented in models used. Contact condition implemented effecting heat flux at contact surface while not at offset surface (b) Figure demonstrating how a more accurate model of the heat flux over the offset could be implemented.

## 6.2 Results Mechanical simulation of the simplified model

Results from the thermo-mechanical simulations are presented, evaluated and discussed in this section. The simplified model was constructed to evaluate numerical stability and modeling settings for OFW.

Mechanical simulations of the rail geometry had severe convergence problems. Typically, simulations would diverge at 0.3 to 0.4 seconds into the forging phase due to excessively distorted elements or very large strain increments. The simulation presented completed the forging phase however, the cooling phase could never be completed and diverged shortly after the contact condition changed to *Rough* in the tangential direction and not allowing separation in the normal direction. It was decided quite early in the project to explore alternative simulation methods. One possible method is evaluated using RFW<sup>1</sup> of pipes in section 4.3.

The visualized results shown in figures 6.14 and 6.15 imply how far simulations are able to run without diverging. Most simulations would diverge if elements reached this level of distortion. The largest total displacement is approximately 13 mm and total displacement are illustrated using a colour scale as shown in figure 6.15d. Due to the shape of the rail profile distortions are the most severe in corner zones shown in figures 6.14c and 6.14d. Using a method where the mesh is continually constructed from the deformed geometry could solve this issue.

Large strain increments are also a cause of concern. The axial displacement is shown in figures 6.16a and 6.16b. In 6.16b it possible to see where the simulation start diverging using the specified process parameters. At approximately 0.35 seconds into the forging phase strain increments are very large. Zones at high temperatures become fully plastic with the load increasing. The load is approximately 130 to 160 MPa when these large strain increments start to cause numerical instability. A visco-plastic material model could aid in reducing the strain increments.

During the heating phase the material expands due to thermal expansion increasing the length of the rail by 0.6 mm with a load of 30 MPa applied, see figure 6.16b.

---

<sup>1</sup>Rotary friction welding

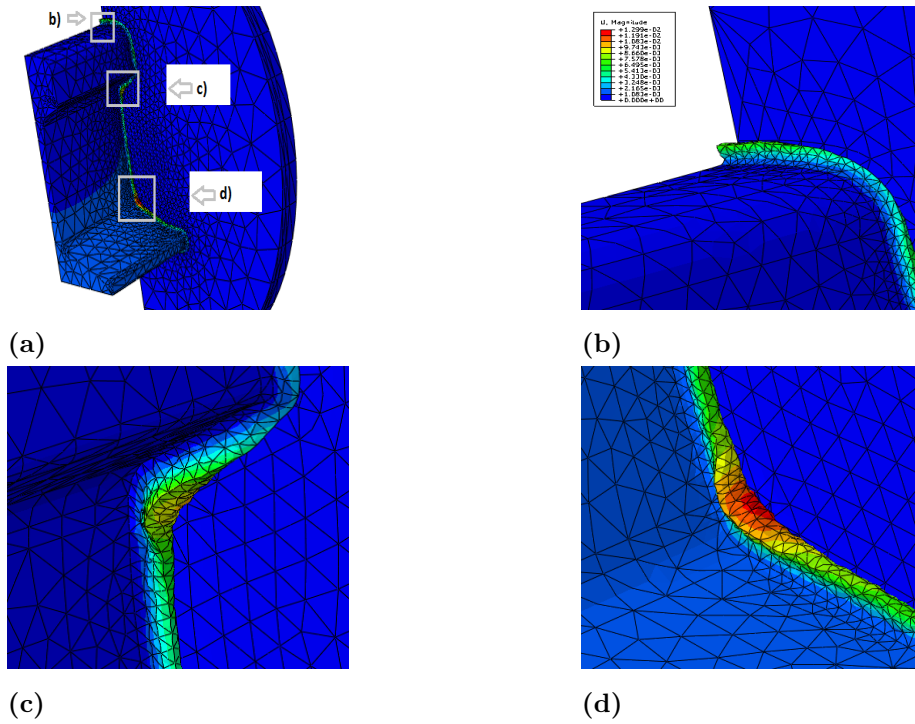


**Figure 6.14:** Visualization of total displacement after the forging phase. (a) Full view. (b) Zoom in at railhead. (c) Zoom in at upper rail curvature. (d) Zoom in at lower rail curvature.

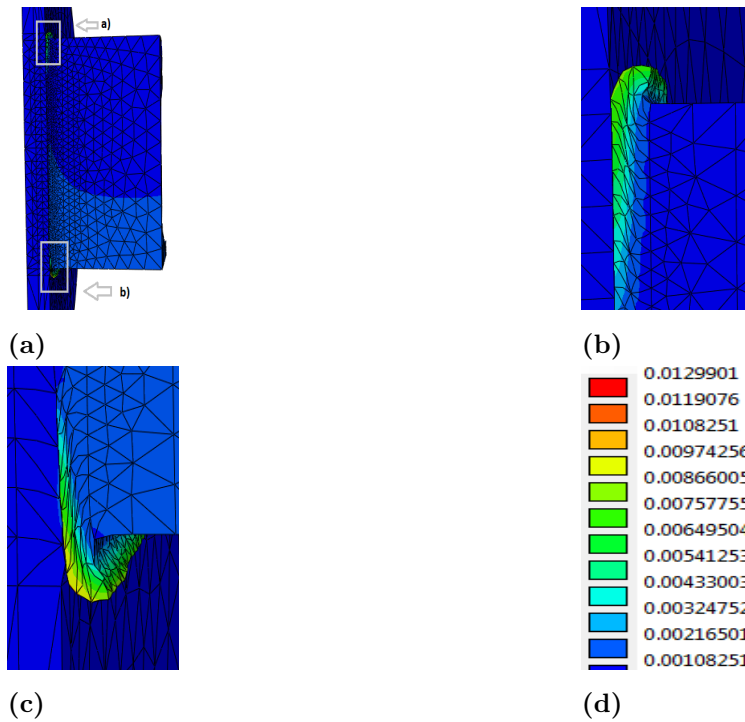


**Figure 6.15:** Visualization of total displacement after the forging phase at x-symmetry surface. (a) Full view. (b) Zoom in at railhead symmetry surface. (c) Zoom in at Railfoot symmetry surface. (d) Specified total displacement in figures.

## 6. Thermal and mechanical results from modeling of orbital friction welding

---

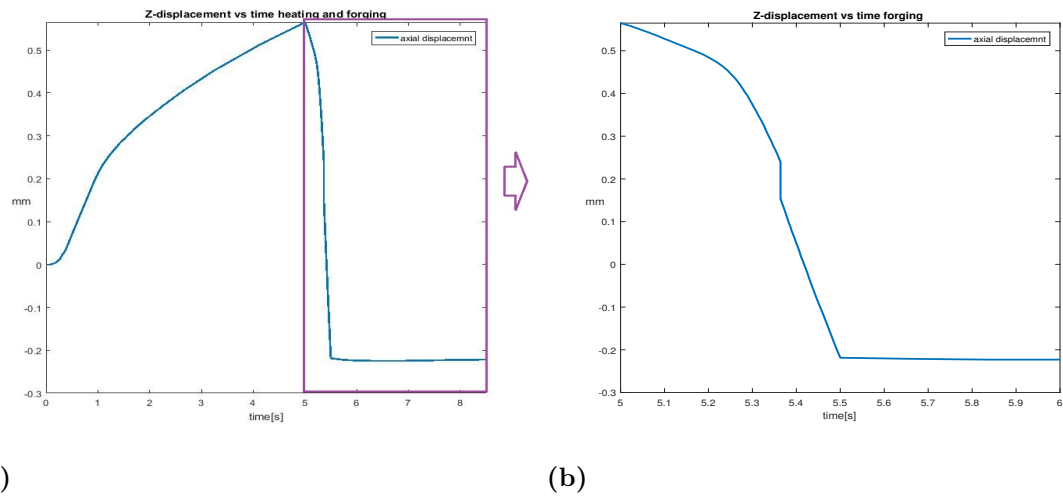


**Figure 6.16:** (a) Axial displacement during heating and forging. (b) Axial displacement during forging

# 7

## Conclusion

The goal of this master thesis was to develop a thermo-mechanical FE-model for the orbital frictional welding (OFW) process of rails. However, due to the complexity of the simulation process several sub-models was analysed in order to improve the understanding of different aspects in the system. Large emphasis has been on evaluating material properties and numerical aspects in addition to how the material micro structure is effected by changes in process parameters and thermal sinks.

### 7.1 Pipe system for evaluation and calibration

Three models concerning rotary friction welding (RFW) of pipes were evaluated in the project. The RFW system is less complex and has been evaluated to a greater extent in other studies compared to OFW. The simulation models can therefore be used to evaluate aspects in material modeling. Specifically, modeling of yield strength and heat flux effects the results.

#### 7.1.1 Heat flux modeling

One of the sub-goals was to deliver a calibrated heat flux model and two possible candidates was proposed for this procedure, the *Tau model* and the *Tri-linear model*. However, due to that experimental data was not delivered during the span of the project this could not be done. Instead a thermal simulation for RFW of pipes was used in order to better understand the heat flux models. This simulation model included the complete pipe geometry and machining clamps.

The proposed *Tau model* is based on the plastic flow rule for pure shear stress. However, it is reasonable to assume that this rule becomes invalid when the material transitions into a more visco-plastic behavior at high temperatures, see Section 3.1. As for the *Tri-linear* model it has been concluded that it is a more convenient model to use when calibrating the heat flux in accordance with experimental data, see Section 4.5. However, this model is fictive as it does not include any physical properties. The friction coefficient is expected to be strongly dependent on the applied load and relative velocity as shown in [7]. It is uncertain whether the *Tri-linear* model will be able to accurately represent systems other than the one it has been calibrated for.

### 7.1.2 Material behavior

Evaluating the material parameters used in previous projects, [1, 4] it was found that the yield model provided unsatisfactory and too stiff responses. Two alternative models was created from literature's studies and evaluated using a simplified thermo-mechanical pipe model as shown in section 3.3.1. These models provided a more realistic response for both simulations using rails and pipes. The response was compared to a experimental case of RFW in section 4.6 as verification.

### 7.1.3 Dealing with mesh distortion

This study found that the limiting factor when simulating friction welding is the mesh. Large deformations are expected for friction welding and this causes the mesh to become distorted. Distorted elements creates large numerical errors and ultimately forces the solution to diverge. In order to deal with the mesh distortion a new methodology was presented. This methodology recreates the model based on the deformed geometry of the previous simulation and restart the process from that point.

Results from using this methodology for the simplified pipe model, see Section 4, closely resembled that of other studies such as [20–22]. It is therefore reasonable to assume that the remeshing methodology could be used in order to accurately evaluate the friction welding process. The methodology show the ability to simulate the large deformations expected in RFW. However, the simulation model showed signs of numerical instability.

To improve the simulation models numerical stability one of the pipes was replaced with a rigid plane. This simplifies the contact condition between the contact surfaces and thus makes it easier for the solver to find a solution. This simulation model proved to be more stable but had issues with the new methodology as solution mapping errors occurred in the remeshed models.

## 7.2 The Rail system for process evaluation

Two models has been evaluated for OFW in order to understand the the effect of process parameters, thermal sinks and investigate the numerical stability of the simulation.

### 7.2.1 Effects of process parameters

The complete system from OFW of rails was created in order to analyse the effect of different process parameters and machine clamps. Overall the results showed that thermal sinks had little impact on the temperature field and cooling rate for most parts of the rail, see section 6.1.3. Cooling rates are dependent on process parameters such as length of the heating phase will decrease the cooling rate. Parts

within the heat affected zone (HAZ) have insignificant differences in cooling rate with respect to a logarithmic scale which was also found in [1].

### **7.2.2 Numerical stability**

A simplified rail geometry was used for the thermo-mechanical simulations of rails. This model experienced many numerical problems which severely limited what process parameters that could be used.

The simulations suffered from severe mesh distortions and these were the main limiting factor in the choice process parameters. The study found that in order to perform these kind of simulations it is necessary to implement some form of remeshing methodology such as the one used for the pipe system.

It was also found that large strain increments cause numerical instability as demonstrated in section 6.2. Visco-plastic behavior is therefore introduced due to numerical reasons. It was showed from RFW simulations that a visco-plastic model stabilized the solution.



# 8

## Future work

### 8.1 Numerical stability

In order to deal with the numerical issues caused by mesh distortion a method for remeshing needs to be developed for 3D geometries. It is therefore recommended that one looks into 3D mesh to mesh solution mapping. In ABAQUS there is a plug-in available for the orphan to mesh conversion, but it has to be requested from its creator. In [27] a similar method has been used for 3D remeshing. It looks promising and could be the solution to the numerical simulation problems.

Numerical issues are also caused by large strain increments which can be reduced by introducing a visco-plastic model. The visco-plastic model is used for numerical reasons but, since steel is to be considered visco-plastic at high temperatures such a model could provide more accurate results.

There could be numerical issues concerning material parameters. The model used in [17] showed far more stable behavior than models from this study.

### 8.2 Thermal modeling

There are many unknowns regarding the modeling of the friction coefficient. Calibrating one of the friction coefficient models would improve its credibility. However, the dependencies of load and relative velocity might make it necessary to calibrate the model for several cases. From there it might be possible to take this dependency into account through interpolation between the cases.

It is recommended to calibrate the heat flux models using experimental data. As an initial calibration a thermal simulation could be used. The calibration is done by adjusting the parameters in the friction models until it yields simulations with a similar temperature field as the experimental tests. With the initial calibration finished the thermo-mechanical model can be used for an additional calibration in order to compensate for the displacements.



# Bibliography

- [1] Wahlstedt, I. (2016) *FE modeling of Orbital friction welding*, Chalmers University of Technology, Gothenburg.
- [2] Bisschop, R., Granlund, M., Kalasho, K., Nordenskold, KNUT. (2016) *Finite Element Analysis on the Application of an Orbital Friction Welding Process to Rails*, Technical report. Chalmers University of Technology, Gothenburg.
- [3] Bisschop, R., Oddy, C. (2016) *Log of Thermal Simulation*, Chalmers University of Technology, Gothenburg.
- [4] Bisschop, R., Oddy, C. (2016) *Log of Mechanical Simulation*, Chalmers University of Technology, Gothenburg.
- [5] Maalekian, M. and Cerjak H. (2008) *Thermal-phase transformation modelling and neural network analysis of friction welding of non-circular eutectoid steel component*, Welding in the world, Volume, 53
- [6] Maalekian, M. (2007) *Friction welding – critical assessment of literature*, Science and Technology of Welding and Joining, 12:8, pp. 738-759
- [7] P. Åström (2002) *Optimization of Parameters in a Friction Model for Friction Welding*, Div. of Computer Aided Design. A Course Assignment in a Course in Engineering Design Optimisation at Linköping University. Tech. rep. Luleå University of Technology, Div. of Computer Aided Design, Oct. 21, 2002.
- [8] *Simulia Abaqus User's Guide*. [Electronic] Release 6.14, Simulia, Inc. <http://abaqus.software.polimi.it/v6.14/index.html> (2016-09-09)
- [9] Ekh, M. (2014) *Mechanics of solids– linear elasticity*. Chalmers University of Technology, Gothenburg. (Course literature)
- [10] Runesson, K., Steinmann, P., Ekh, M., Menzel, A. (2005) *Constitutive modeling of engineering materials- Theory and computation*. Seventh edition, Chalmers University of Technology, Gothenburg. (Course literature)
- [11] *Innovative Welding Processes for New Rail Infrastructures* (2016),[online] <http://www.wrist-project.eu/> [2016-09-09]
- [12] Brouzoulis, J., Josefson, Lennart. (2015) *Innovative Welding Processes for New Rail Infrastructures*, Technical report, Chalmers University of Technology, Gothenburg.
- [13] A. Skyttebol, B.L. Josefson, J.W. Ringsberg (2003) *Fatigue crack growth in a welded rail under the influence of residual stresses*, Chalmers University of Technology, Gothenburg. Engineering Fracture Mechanics, 72, pp. 271–285.
- [14] Y. Chen, F. Lawrence, C. Barkan, and J. Dantzig (2003) *Heat transfer modelling of rail thermite welding*, Proc. IMechE Volume, 220 Part F:J, pp. 207-217.
- [15] The European Union (2005) *Eurocode 3: Design of steel structures*.

- [16] M. Soucail, A. Moal, L. Naze, E. Massoniz C. Levailant and Y. Bienvenu (1992) *Microstructural study and numerical simulation of inertia. Friction welding of astroloy*. The minerals, metals and materials society, 1992.
- [17] Dassault-systems, ed. *Abaqus 6.13, Example problem guide; 1.3.18 Inertia welding simulation using Abaqus/Standard and Abaqus/CAE*, [online], Release 6.13, Simulia, Inc. <http://abaqus.software.polimi.it/v6.13/index.html> (2016-09-09)
- [18] Dassault-systems, ed. *Abaqus 6.13, Theory guide; 3.2.3 Hybrid incompressible solid element formulation*, [online], Release 6.13, Simulia, Inc. <http://abaqus.software.polimi.it/v6.13/index.html> (2016-09-09)
- [19] Dassault-systems, ed. *Abaqus 6.13, User's guide; 27 Elements*, [online], section 27.1, Release 6.13, Simulia, Inc. <http://abaqus.software.polimi.it/v6.13/index.html> (2016-09-09)
- [20] A. Moal and E. Massoni (1995) *Finite element simulation of the inertia welding of two similar parts*, Engineering Computations, volume, 12, Issue, 6, pp. 497-512
- [21] L. Wang, M. Preuss, P.J. Baxter, and P. Wilson (2005) *Energy input based Finite element process modeling of inertial welding*, Metallurgical and Materials Transactions, ProQuest Central, volume, 36B, Issue, 4, pp. 513-523
- [22] L. D'Alvise, E. Massoni, S.J. Walløe (2002) *Finite element modelling of the inertia friction welding process between dissimilar materials*, Journal of Materials Processing Technology 125–126, pp. 387–391
- [23] V. Gantchenko, P. Jouinot, A. Köster (2008) *Viscoplastic behaviour of metals deformed at high-temperature, application to tension–compression cycles*, J Mater Sci, volume, 43, pp. 5342–5349
- [24] A. Ambroziak, M. Winnicki, P. Laska, M. Lachowicz, M. Zwierzchowski, J. Lesniewski (2011) *Examination of friction coefficient in friction welding process of tubular steel elements*, Archives of metallurgy and materials, Volume, 56, Issue, 4, pp. 975-980
- [25] K. Faes *Experimental plan to calibrate the heat generation model to simulate the orbital friction welding process*, WRIST-project.
- [26] MTIwelding [image] available at: <http://www.mtiwelding.com/wp-content/uploads/2015/10/9.jpg> [2017-01-14]
- [27] Wenya Li, Feifan Wang, Shanxiang Shi, Tiejun Ma, Jinglong Li, and Achilleas Vairis (2011) *3D Finite element analysis of the effect of process parameters on linear friction welding of mild steel*, JMEPEG volume, 23, pp. 4010–4018

# A

## Remeshing PYTHON script

*#PYTHON script created in order to use mesh to mesh solution mapping.  
#This script utilises functions from [18]*

```
import os, sys, re, osutils
import driverUtils, sys
from driverConstants import *
from abaqusConstants import *
from driverExceptions import *
from driverStandard import StandardAnalysis
from analysis import AnalysisApplication
sys.path.append(os.getcwd())
from inertiaWeld_utils import *
import uti

print "remesh_buildTD19.py"
platform = uti.getPlatform()
#####
#UserInput
meshSize          = 0.0005
nearWeldMeshSize  = 0.00005
distortionLimit   = 0.8
nearWeldZone      = 0.004
remeshFeatureAngle = 10.0
simulationTime     = 3
PressureFriction   = 30000000
PressureWeld       = 150000000
TimeFriction1      = 0.5
TimeFriction2      = 3
TimeWeld1          = 3.5
TimeWeld2          = 6
#Remesh job
primaryJobName     = 'pipeweldTD'
ancestorJobName    = 'pipeweldTD_remesh_6'
#TimeStuff
totalTime          = 0.1572+0.2646
RemeshSTEP         = 0
```

## A. Remeshing PYTHON script

---

```
RemeshINC      = 500
remeshNumber   = 7
RunTime = 3 + totalTime
```

```
#NOTES
```

```
#_remesh_i
```

```
#In code:      initial = -1, step-1 = 0, step-2 = 1...
```

```
#In keywords: initial = 0, step-1 = 1, step-2 = 2...
```

```
#####
```

```
vp1 = session.Viewport(name='Viewport:□1')
vp1.makeCurrent()
session.viewports['Viewport:□1'].maximize()
```

```
#Opening the primary CAE
```

```
Mdb()
openMdb(primaryJobName + '.cae')
mdb.saveAs(primaryJobName + '.cae')
```

```
remeshJobName = newJobName(primaryJobName, remeshNumber)
```

```
#Creating the new remesh CAE
```

```
mdb.saveAs(remeshJobName + '.cae')
openMdb(remeshJobName + '.cae')
```

```
model=mdb.models['Model-1']
a = model.rootAssembly
```

```
try:
```

```
    a.deleteFeatures(('Datum□plane-1', 'Partition□face-1', ))
```

```
except:
```

```
    pass
```

```
try:
```

```
    a.deleteFeatures(('Datum□plane-2', 'Partition□face-2', ))
```

```
except:
```

```
    pass
```

```
# Replace the pipes with the deformed configuration outlines
```

---

```

updateGeometry( 'PipeT', 'PIPET-1', ancestorJobName + '.odb',
    remeshFeatureAngle, RemeshSTEP, RemeshINC)
updateGeometry( 'PipeB', 'PIPEB-1', ancestorJobName + '.odb',
    remeshFeatureAngle, RemeshSTEP, RemeshINC)
from part import *
from assembly import *
a = model.rootAssembly
try:
    del a.features[ 'Coincident□Point-1' ]
except:
    pass
a.backup()
a.regenerate()

## Re-establish attributes
# materials
from caeModules import *
p = model.parts[ 'PipeT' ]
f = p.faces
faces = f.getSequenceFromMask(mask=('[#1□]', ), )
region = regionToolset.Region(faces=faces)
p = model.parts[ 'PipeT' ]
p.SectionAssignment(region=region, sectionName='Section-2',
    offset=0.0)
p = model.parts[ 'PipeB' ]
session.viewports[ 'Viewport:□1' ].setValues(displayedObject=p)
p = model.parts[ 'PipeB' ]
f = p.faces
faces = f.getSequenceFromMask(mask=('[#1□]', ), )
region = regionToolset.Region(faces=faces)
p = model.parts[ 'PipeB' ]
p.SectionAssignment(region=region, sectionName='Section-1',
    offset=0.0)

# sets
from assembly import *
lowestEdgeSet(model.rootAssembly, 'PipeB-1', 'B_LoadingAttachment')
faces1 = a.instances[ 'PipeB-1' ].faces.getSequenceFromMask(
    mask=('[#1□]', ), )
a.Set(faces=faces1, name='B_PipeBody')
faces2 = a.instances[ 'PipeT-1' ].faces.getSequenceFromMask(
    mask=('[#1□]', ), )
a.Set(faces=faces2, name='T_PipeBody')

```

```

# surfaces
lowestSurface('PipeB-1', 'B_LoadingSurface')
perimeterSurface('PipeB-1', 'B_PipeSurface')
perimeterSurface('PipeT-1', 'T_PipeSurface')
#####

# Redefine the step
timeRemaining = simulationTime - totalTime

from step import *
model.steps['Weld□step'].setValues(
    description='Weld□step', timePeriod=timeRemaining,
    maxInc=timeRemaining, initialInc=1.e-5, minInc=2e-08)
try:
    del model.predefinedFields['Predefined□Field-1']
except:
    pass

# Modifying load
if RunTime <= TimeFriction1:
    P = PressureFriction /
        (TimeFriction2 - TimeFriction1) * RunTime
    del model.amplitudes['Amp-1']
    model.TabularAmplitude(name='Amp-1', timeSpan=STEP,
smooth=SOLVER_DEFAULT, data=((0.0, P),
    (TimeFriction1 - RunTime, PressureFriction),
    (TimeFriction2 - RunTime, PressureFriction),
    (TimeWeld1 - RunTime, PressureWeld),
    (TimeWeld2 - RunTime, PressureWeld)))
elif RunTime <= TimeFriction2 and RunTime > TimeFriction1:
    del model.amplitudes['Amp-1']
    model.TabularAmplitude(name='Amp-1', timeSpan=STEP,
smooth=SOLVER_DEFAULT, data=((0.0, PressureFriction),
    (TimeFriction2 - RunTime, PressureFriction),
    (TimeWeld1 - RunTime, PressureWeld),
    (TimeWeld2 - RunTime, PressureWeld)))
elif RunTime <= TimeWeld1 and RunTime > TimeFriction2:
    P = (PressureWeld - PressureFriction) / (TimeWeld1 - TimeFriction2) *
        (RunTime - TimeFriction2)
    del model.amplitudes['Amp-1']
    model.TabularAmplitude(name='Amp-1', timeSpan=STEP,
smooth=SOLVER_DEFAULT, data=((0.0, P),
    (TimeWeld1 - RunTime, PressureWeld),
    (TimeWeld2 - RunTime, PressureWeld)))

```

---

```

elif RunTime <= TimeWeld2 and RunTime > TimeWeld1:
    del model.amplitudes[ 'Amp-1' ]
    model.TabularAmplitude(name='Amp-1', timeSpan=STEP,
smooth=SOLVER_DEFAULT, data=((0.0, PressureWeld),
(TimeWeld2-RunTime, PressureWeld)))
else:
    del model.amplitudes[ 'Amp-1' ]
    model.TabularAmplitude(name='Amp-1', timeSpan=STEP,
smooth=SOLVER_DEFAULT, data=((0.0, 0.0)))

# mesh
# Find the highest point on the lower pipe
e = a.instances[ 'PipeB-1' ].edges
v = a.instances[ 'PipeB-1' ].vertices
highestLocation = -99999
for k in range(len(v)):
    ((x,y,z),) = v[k].pointOn
    if y > highestLocation:
        highestLocation = y
lowerCutPosition = highestLocation-nearWeldZone
lowerCutPosition = sliceBottomInstance( 'PipeB-1', lowerCutPosition)

# Find the lowest point on the top pipe
e = a.instances[ 'PipeT-1' ].edges
v = a.instances[ 'PipeT-1' ].vertices
upperCutPosition = 0
lowestLocation = 99999
for k in range(len(v)):
    ((x,y,z),) = v[k].pointOn
    if y < lowestLocation:
        lowestLocation = y
upperCutPosition = nearWeldZone+lowestLocation
upperCutPosition = sliceTopInstance( 'PipeT-1', upperCutPosition)

removeEdgeSeeds( 'PipeB-1' )
removeEdgeSeeds( 'PipeT-1' )

print( " !!!TODO" )
print( " !!! predefinedFields !!! " )
print( " !!!MESH!!! " )
print( " !!! Ensure that the sets and surfaces are correct !!! " )
print( " !!! *MAP SOLUTION, STEP=step, INC=increment !!! " )

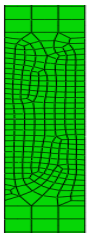
## Add keywords

```

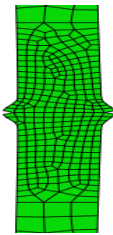
```
import job
from job import *
model.keywordBlock.synchVersions()
model.keywordBlock.setValues(edited = 0)
model.keywordBlock.synchVersions()
modelBlock = whereIsLastBlock("*Step") - 1
model.keywordBlock.insert(modelBlock, """*map solution, step=,
    inc=""")
historyBlock = whereIsLastBlock("*End□Step") - 1
model.keywordBlock.insert(historyBlock,
    """*controls, analysis=discontinuous """)
mdb.models['Model-1'].setValues(noPartsInputFile=OFF)
mdb.jobs.changeKey(fromName=primaryJobName, toName=remeshJobName)
#mdb.jobs[remeshJobName].writeInput()
#mdb.save()
```

# B

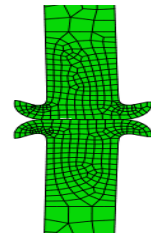
## Pipe remeshing, Results



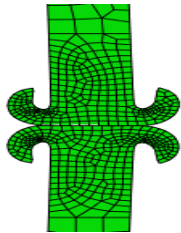
(a) Heating phase,  
time = 0s



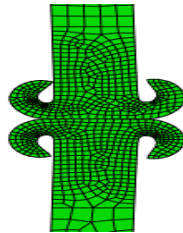
(b) Heating phase,  
time = 1.05s



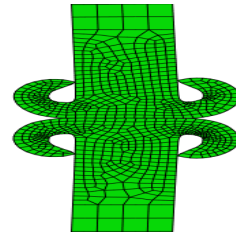
(c) Heating phase,  
time = 2.12s



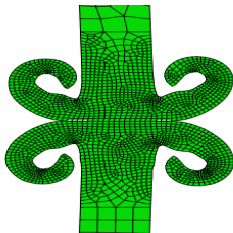
(d) Heating phase,  
time = 2.47s



(e) Forging phase,  
time = 3s



(f) Forging phase,  
time = 3.2s



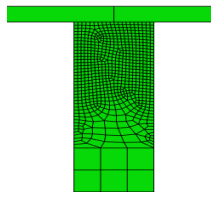
(g) Forging phase,  
time = 6s

**Figure B.1:** 2 pipe model: Flash formations when using the mesh to mesh remeshing method

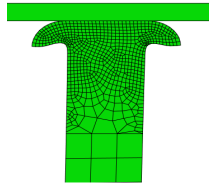


# C

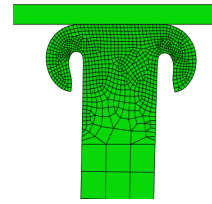
## Pipe remeshing, Results



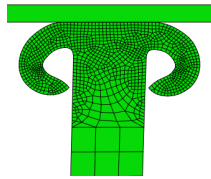
(a) Heating phase,  
time = 0s



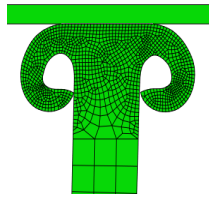
(b) Heating phase,  
time = 1.8s



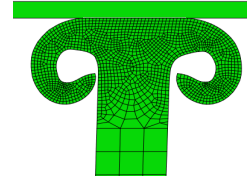
(c) Heating phase,  
time = 2.3s



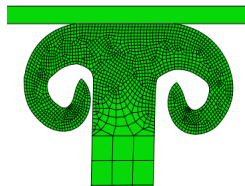
(d) Forging phase,  
time = 3s



(e) Forging phase,  
time = 3.2s



(f) Forging phase,  
time = 3.3s



(g) Forging phase,  
time = 6s

**Figure C.1:** rigid plane model: Flash formations when using the mesh to mesh remeshing method



# D

## Thermal Results

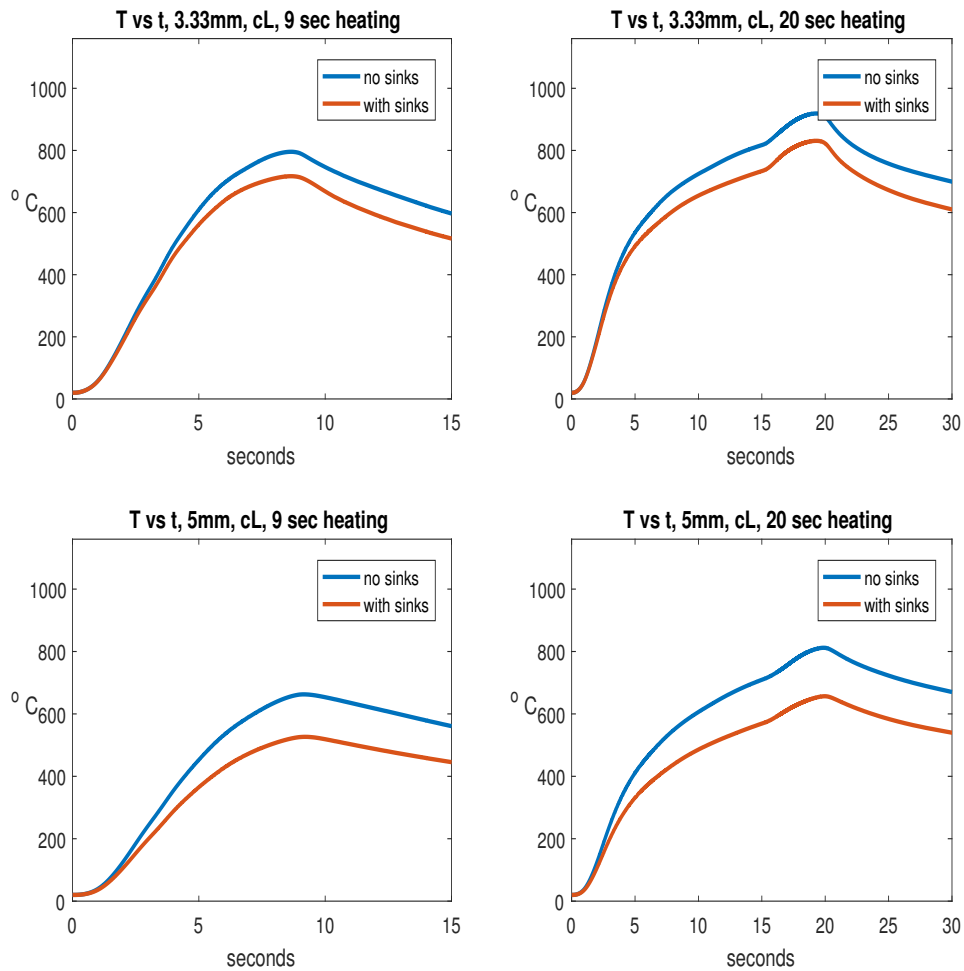


**Figure D.1:** Time vs temperature, T1, T2, T4 and T5 (with and without sinks) at nodes on cL located 3.33mm and 5mm from the disc. Node located at 5mm from the disc is in contact with the clamp.

## D. Thermal Results

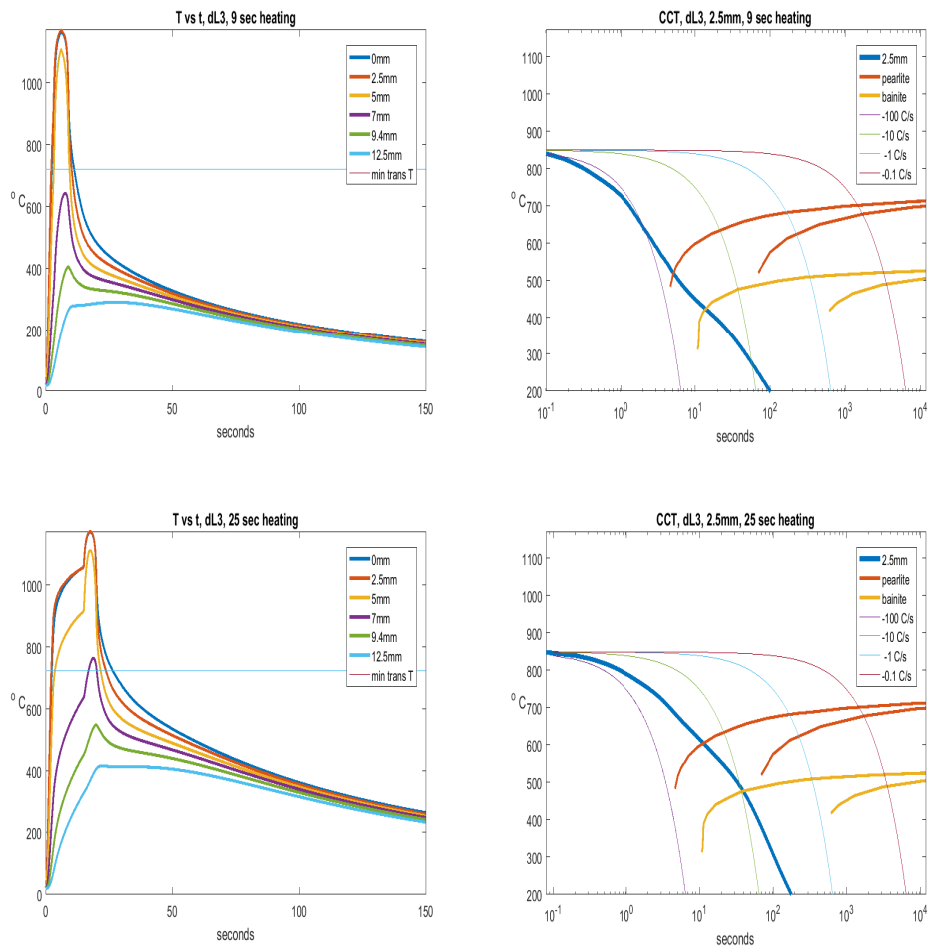


**Figure D.2:** Results from simulation with sinks for 9 and 25 seconds long heating phase at nodes located on dL3

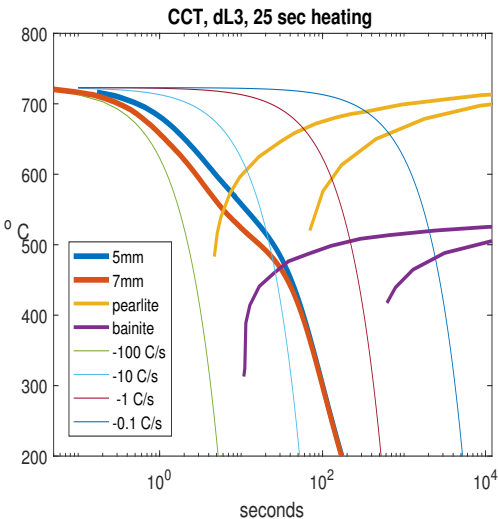


Figure D.3: Results from simulation with sinks for 25 seconds long heating phase at nodes located on dL3, demonstrating the difference in cooling rate between nodes located at 5 and 7mm from starting point of dL3

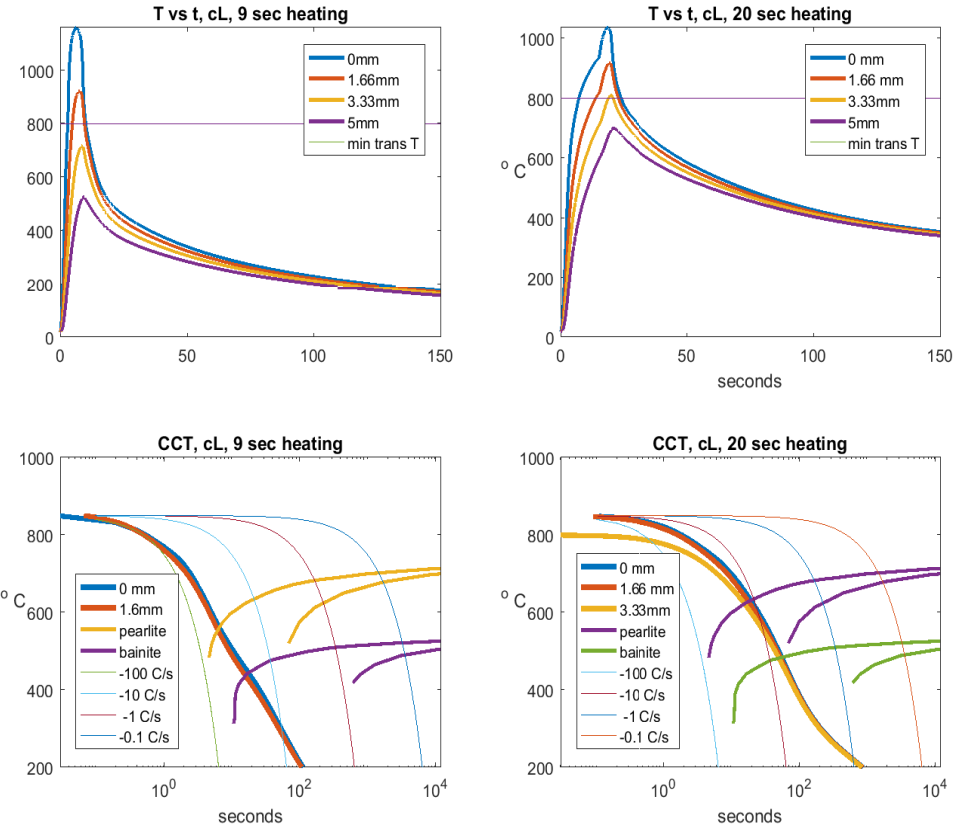
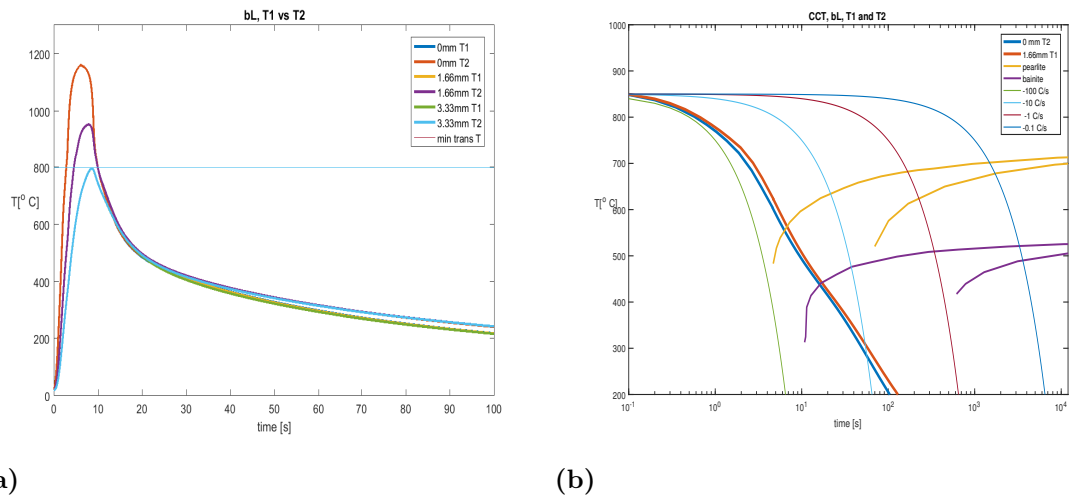
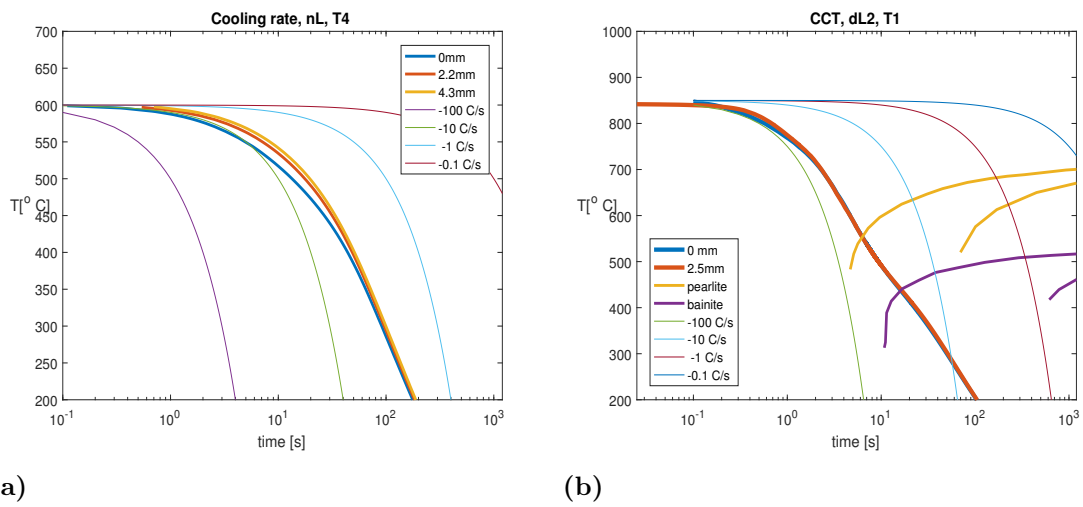


Figure D.4: Results regarding material evaluation along cL, clamp is located at 5mm

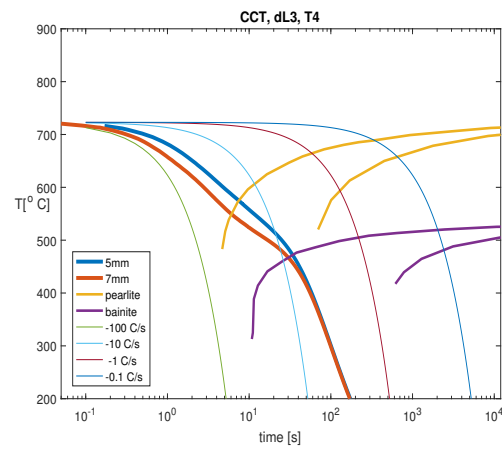
## D. Thermal Results



**Figure D.5:** Figure results from simulations T1 and T2 are presented for nodes along bL with the aim to evaluate the general effect of the rail clamp. a) Temperature variation for nodes along bL to determine size of the HAZ. b) CCT diagram demonstrating the effect on the cooling rate of the rail clamp



**Figure D.6:** (a) Temperature variation along dL2 for simulation T1 (b) CCT diagram comparing cooling rates at different nodes along dL2 for simulation T1.



1

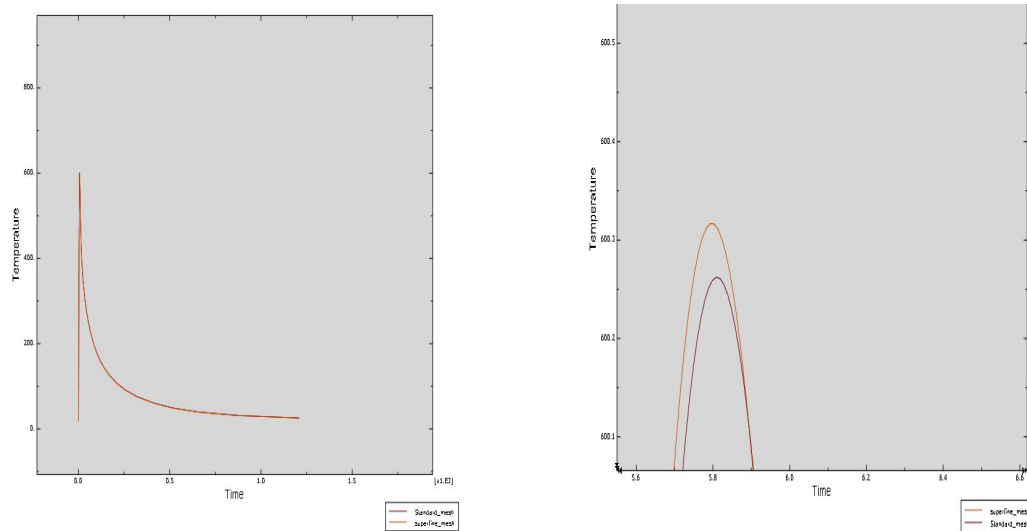
**Figure D.7:** CCT diagram comparing cooling rates at different nodes along dL3 for simulation T4.



# E

## Mesh convergence

A mesh convergence study was performed for thermal modelling of the full model by comparing the standard mesh with super fine mesh using minimum sidelength of 0.6mm for elements. The results were almost identical implying mesh convergence.



(a) Temperature vs t comparing standard mesh to superfine mesh (b) Temperature vs t comparing standard mesh to superfine mesh

**Figure E.1:** Mesh convergence



# F

## Material parameters

EC3 & Skyttebol: Final Linear Kinematic model						F
H factor	Sigma_y	eps	T			
	430000000	0	20	K H i a n r e d m e n t i n g	N o  A n n e l i n g	1
1.766109	759426948	0.03	20			
	430000000	0	400			1
1.6	688000000	0.03	400			
	242000000	0	600			0.56
1.437	347754000	0.03	600			
	989000000	0	700		0.23	
1.1	108790000	0.03	700			
	47300000	0	800	I d e a l l y  P l a s t i c	A n n e a l i n g	0.11
1	47300000	0.03	800			
	25800000	0	900			0.06
1	25800000	0.03	900			
	17200000	0	1000			0.04
1	17200000	0.03	1000			
	8600000	0	1100			0.02
1	8600000	0.03	1100			
	5000000	0	1470			0.02
1	5000000	0.03	1470			

Figure F.1

F. Material parameters

Reduced stiffness at high temperatures, Strain rate model, Smoothend also known as the Soucal model									
H factor	EC3 & Skyttebol: Final Linear Kinematic model						Reduction F	Gradient MPa/C	Rate factor
	Sigma	eps	eps_dot	T					
	430000000	0	0	20			1	0	1
	451623528.7	0	50	20					1.050287276
	452620661.1	0	100	20					1.052606189
	466077497.2	0	1000000	20					1.083901156
1.766109	759426948	0.03	0	20					1
	797616460.5	0.03	50	20					1.050287276
	799377505.3	0.03	100	20					1.052606189
	823143747.1	0.03	1000000	20					1.083901156
	430000000	0	0	400			1	-0.94	1
	580843770.5	0	50	400					1.350799466
	588746394.5	0	100	400					1.369177662
	704539232.1	0	1000000	400					1.63846333
1.6	688000000	0.03	0	400					1
	929350032.8	0.03	50	400					1.350799466
	941994231.1	0.03	100	400					1.369177662
	1127262771	0.03	1000000	400					1.63846333
	242000000	0	0	600			0.56	-1.431	1
	457659561.8	0	50	600					1.891155214
	470953783.8	0	100	600					1.946090016
	688989759.5	0	1000000	600					2.847065122
1.437	347754000	0.03	0	600					1
	657656790.3	0.03	50	600					1.891155214
	676760587.3	0.03	100	600					1.946090016
	990078284.4	0.03	1000000	600					2.847065122
	98900000	0	0	700			0.23	-0.516	1
	215355818.7	0	50	700					2.177510806
	223291546	0	100	700					2.257750718
	365115373.9	0	1000000	700					3.691763133
1.1	108790000	0.03	0	700					1
	236891400.6	0.03	50	700					2.177510806
	245620700.6	0.03	100	700					2.257750718
	401626911.2	0.03	1000000	700					3.691763133
	47300000	0	0	800			0.11	-0.272089	1
	47300000	0	0.00001	800					1
	146975849.9	0	50	800					3.107311837
	154657653.5	0	100	800					3.269717833
	304352352.6	0	1000000	800					6.434510625
	20091100	0	0	900			0.046723488	-0.109273204	1
	20091100	0	0.00001	900					1
	126867000	0	50	900					6.314587056
	137820000	0	100	900					6.859753821
	414194000	0	1000000	900					20.61579505
	4668280	0	0	1041.14			0.010856465	-0.034457931	1
	4668280	0	0.00001	1041.14					1
	78888600	0	50	1041.14					16.89885782
	89575700	0	100	1041.14					19.18815924
	484565000	0	1000000	1041.14					103.7994722
	1310010	0	0	1138.6			0.003046535	-0.005498951	1
	1310010	0	0.00001	1138.6					1
	42125400	0	50	1138.6					32.15654842
	49235200	0	100	1138.6					37.58383524
	391089000	0	1000000	1138.6					298.5389425
	817139	0	0	1228.23			0.001900323	-0.009397195	1
	817139	0	0.00001	1228.23					1
	26276300	0	50	1228.23					32.15646298
	30711100	0	100	1228.23					37.58369139
	243947000	0	1000000	1228.23					298.5379476
	33225	0	0	1311.65			7.72674E-05	-0.00020982	1
	33225	0	0.00001	1311.65					1
	33301000	0	50	1311.65					1002.287434
	45426700	0	100	1311.65					1367.244545
	281333000	0	1000000	1311.65					84675.09406
	0.001	0	0	1470			2.32558E-12		1
	0.001	0	0.00001	1470					1
	500000	0	50	1470					500000000
XX	1000000	0	100	1470					1000000000
	1000000000	0	1000000	1470					1E+12

Figure F.2